

Circular RNA-Encoded MET Variant Is a Targetable Factor in Glioblastoma

Jian Zhong

First Affiliated Hospital of Sun Yat-sen University

Xujia Wu

First Affiliated Hospital of Sun Yat-sen University

Junju Chen

First Affiliated Hospital of Sun Yat-sen University

Yixin Gao

First Affiliated Hospital of Sun Yat-sen University

Maolei Zhang

First Affiliated Hospital of Sun Yat-sen University

Huangkai Zhou

Northeast Institute of Geography and Agroecology

Jia Yang

First Affiliated Hospital of Sun Yat-sen University

Feizhe Xiao

First Affiliated Hospital of Sun Yat-sen University

Xuesong Yang

First Affiliated Hospital of Sun Yat-sen University

Nunu Huang

First Affiliated Hospital of Sun Yat-sen University

Xiuxing Wang

National Health Commission Key Laboratory of Antibody Techniques, Jiangsu Provincial Key Laboratory of Human Functional Genomics, Collaborative Innovation Center for Personalized Cancer Medicine

Nu zhang (✉ zhangnu2@mail.sysu.edu.cn)

First Affiliated Hospital of Sun Yat-sen University <https://orcid.org/0000-0002-2817-7065>

Article

Keywords: MET, HGF, Circular RNA, MET404, Glioblastoma, m6A, YTHDF2

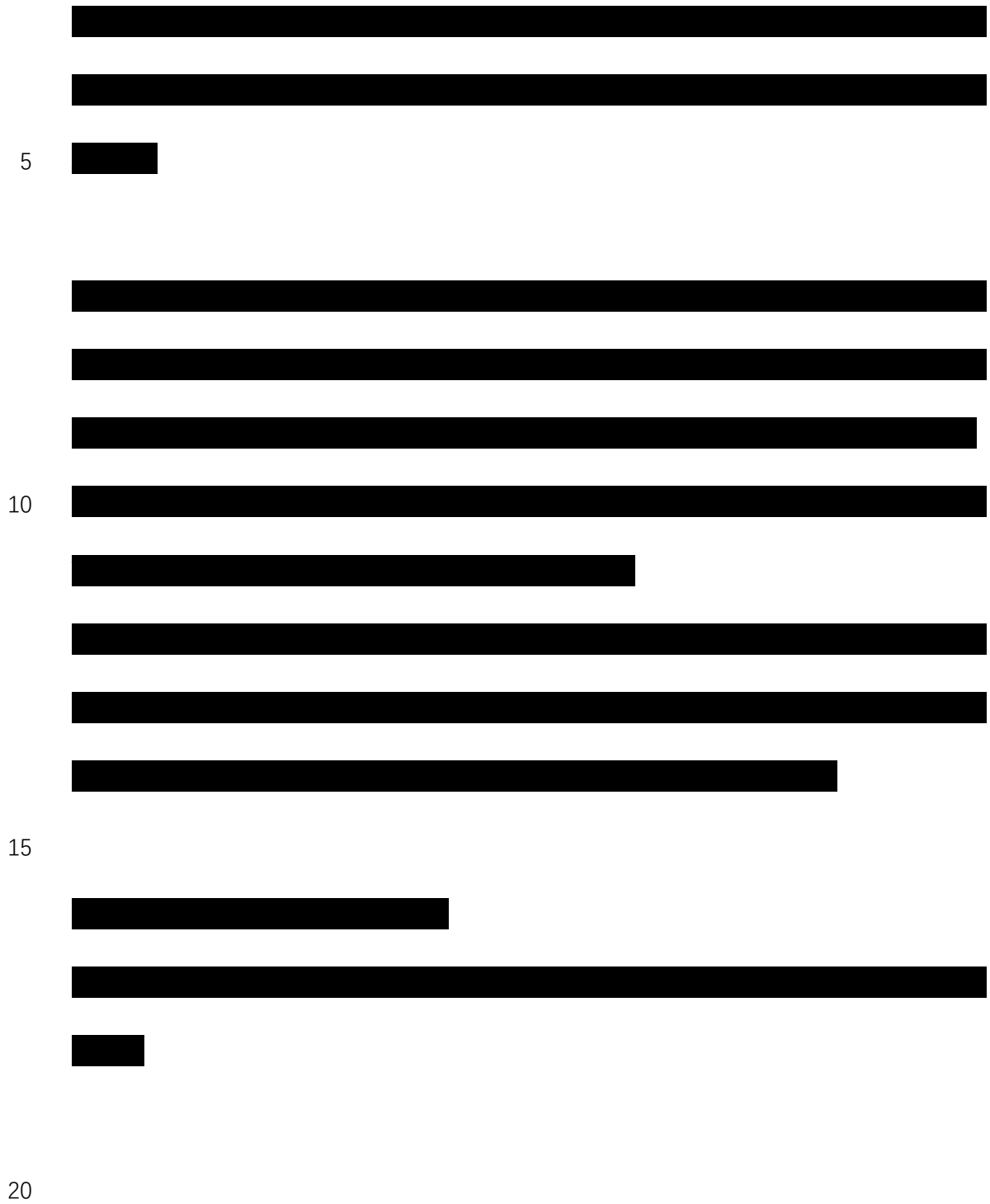
Posted Date: June 28th, 2022

DOI: <https://doi.org/10.21203/rs.3.rs-1730428/v1>

License: © ⓘ This work is licensed under a Creative Commons Attribution 4.0 International License.

[Read Full License](#)

Circular RNA-Encoded MET Variant Is a Targetable Factor in Glioblastoma



ABSTRACT

Activated by its single ligand, hepatocyte growth factor (HGF), the receptor tyrosine
25 kinase MET is pivotal in promoting glioblastoma stem cell (GSC) self-renewal,
invasiveness and tumorigenicity. Nevertheless, HGF/MET-targeted therapy has shown
limited clinical benefits in glioblastoma patients, suggesting hidden mechanisms of
MET signalling in glioblastoma. Here, we show that circular MET RNA (circMET)
encodes a 404 amino acid novel MET variant (MET404) facilitated by the N⁶-
30 methyladenosine (m⁶A) reader YTHDF2. Genetic ablation of circMET inhibited
MET404 expression in mice and attenuated MET signalling. Conversely, MET404
knock-in plus *P53* knock-out in mouse astrocytes initiated glioblastoma tumorigenesis
and shortened overall survival. MET404 directly interacts with the MET β subunit and
forms a constitutively activated MET receptor whose activity does not require HGF
35 stimulation. High MET404 expression predicts poor prognosis in glioblastoma patients,
indicating its clinical relevance. Targeting MET404 through a neutralizing antibody or
genetic ablation reduced glioblastoma tumorigenicity *in vitro* and *in vivo*, with
combinatorial benefits when a traditional MET inhibitor was added. Overall, we
identified a novel MET variant that promotes glioblastoma tumorigenicity, offering a
40 potential new therapeutic strategy for glioblastoma.

KEY WORDS

MET; HGF; Circular RNA; MET404; Glioblastoma; m⁶A; YTHDF2

45 INTRODUCTION

Glioblastoma (GBM), the most commonly seen WHO grade IV primary brain cancer, is virtually incurable even with multimodal treatments, including surgery, radiotherapy and chemotherapy¹. In the past decade, the median survival of GBM patients has remained approximately 12-15 months despite the utilization of novel approaches, including small molecule target therapy and immunotherapy²⁻⁴. GBM displays remarkable intratumoural heterogeneity, bearing multiple genetic or epigenetic alterations, such as loss of *PTEN* and *P53*; amplification of receptor tyrosine kinases (RTKs); inactivation of *CDKN2A* (p16/INK4A) and *CDKN2B*; and mutations in isocitrate dehydrogenase 1 and 2 (*IDH1/2*)⁵. Of note, a high level of *MET* amplification is found in ~4% of GBM tumours. A considerable proportion of GBM tumours with amplification of *EGFR* have aberrant *MET* expression⁶, and activated *MET* signalling is more commonly seen in secondary GBM⁷. Nevertheless, combined onartuzumab/bevacizumab targeted therapy displayed no benefit to GBM patients in phase II clinical trials⁸, indicating the necessity of an in-depth study of *MET* signalling in GBM.

Circular RNAs (circRNAs), previously recognized as noncoding RNAs, have been shown to generate novel molecular targets in human cancers, including GBM⁹⁻¹². Driven by an internal ribosomal entry site (IRES) or N⁶-methyladenosine (m⁶A) modification, circRNAs can encode functional peptides or proteins to influence cancer stem cells (CSCs) in terms of self-renewal, invasion and therapeutic resistance^{9,10,13,14}. Of note, the m⁶A reader YTHDF2 was reported to be highly expressed and maintain the

oncogene characteristics of glioma stem cells (GSCs)¹⁵, highlighting the potential novel therapeutic targets generated from m⁶A-modified circRNAs.

Here, we identified circular MET RNA (circMET) as a m⁶A-modified coding
70 circRNA in GBM. Using genetic models, we demonstrated that circMET encoded a novel protein, MET404, that drives GBM tumorigenesis and revealed that the MET404/MET β subunit formed a chimeric MET receptor, which constitutively activated downstream effectors independent of HGF stimulation. The combination of onartuzumab and MET404 antibody maximally inhibited mouse GBM xenograft
75 progression and prolonged mouse overall survival, highlighting the future translational prospects of targeting MET404 in GBM.

RESULTS

80 *CircMET is a potential coding circRNA subjected to m⁶A modification*

Many protein-coding circRNAs are driven by m⁶A modification^{14,16}. To discover m⁶A -modified circRNAs, we performed RNA-seq and m⁶A -seq in 10 surgical resected GBM samples (Fig. 1a). A total of 1,425 m⁶A -modified circRNAs were identified, of which 1,005 (70.5%) were found by total RNA-seq (17,733) (Fig. 1b, Supp Table 1).
85 Compared with non-m⁶A-modified circRNAs, m⁶A-modified circRNAs were more likely generated from a single exon (18.71% vs. 5.16%) and were more highly expressed in cancerous tissues (Fig. 1c and Extended Data Fig. 1a). Notably, the source genes of m⁶A-modified circRNAs were enriched in multiple RTK pathways (Fig. 1d,

Supp Table 2). Recent studies have revealed that m⁶A modifications can function as
90 internal ribosome entry sites (IRESs), which facilitate binding between circRNAs and
ribosomes, thus promoting their coding potential¹⁴. Next, we performed ribosome
nascent chain sequencing (RNC-seq, capable of detecting circRNAs directly binding to
ribosomes¹⁷) in five patient-derived GSCs and two control neural stem cells (NSCs) to
reveal circRNAs with coding potential. We identified a total of 1,605 differentially
95 expressed RNC-circRNAs ($\log_2FC > 2$, $p < 0.05$), with 349 upregulated and 1,256
downregulated in GSCs (Fig. 1e, Supp Table 3). Among the 1,425 m⁶A-modified
circRNAs identified above, 89 were differentially expressed between GSCs and NSCs
by RNC-seq (Diff_RNC- m⁶A-circRNA). Binding to ribosomes does not ensure that an
RNA can be translated¹⁸; however, YTHDF m⁶A readers were reported to facilitate the
100 initiation of RNA translation^{14,19}. Specifically, YTHDF2, compared with YTHDF1/3,
showed a stronger correlation with GBM prognosis and GSC maintenance¹⁵. To further
narrow down translatable circRNAs in GSCs, we next performed YTHDF2 RNA
immunoprecipitation sequencing (RIP-seq) in GSC456 and GSC23 patient-derived
GSCs and cross-referenced the data with the above m⁶A-seq and RNC-seq results. We
105 detected a total of 255 YTHDF2-associated circRNAs (Fig. 1f, Supp Table 4), of which
five overlapped in the aforementioned 89 Diff_RNC- m⁶A-circRNAs. To here, we
identified five candidate circRNAs, namely, circMET, circSPECC1, circXYLT1,
circCDYL and circRBM33 (Fig. 1g). Given the critical role of MET in GBM
tumorigenesis^{6,7,20,21}, we focused on circMET (hsa_circ_0082002) for further
110 investigation.

CircMET encodes the novel protein MET404

CircMET is formed from exon 2 of the *hMET* gene (Fig. 2a) and is highly conserved in mice (exon 3 of *mMET*, Extended Data Fig. 1b, c). We validated circMET (1214 nt) by using junction-specific primers (Fig. 2a) and tested its circRNA characteristics, including RNase R digestion (Extended Data Fig. 1d), random/oligo dT primer amplification (Extended Data Fig. 1e), half-life (Extended Data Fig. 1f), cellular localization (Extended Data Fig. 1g), and relative expression in several GBM cells and GSCs (Extended Data Fig. 1h). CircMET is a cytoplasm-localized circRNA (Extended Data Fig. 1g, i) and is highly expressed in GSCs compared with NSCs and normal human astrocytes (NHAs) (Extended Data Fig. 1h). By m⁶A-IP, we further validated extensive m⁶A modification of circMET (Fig. 2b), in accordance with the Transcirc database²² (Extended Data Fig. 2a). Ribosome fragment analysis showed that circMET was detected in the heavy polysome fraction, which also supported the translational potential of circMET (Extended Data Fig. 2b). Furthermore, circMET contains a cross-species conserved ORF, which encodes a 404 amino acid (a.a.) protein in both humans and mice (Fig. 2b, left and Extended Data Fig. 2c, d). We termed this novel protein MET404, and a MET404 antibody targeting the C-terminus was also synthesized and tested (Extended Data Fig. 2c, e). MET404 is a membrane- and cytoplasm-localized protein, as determined by immunofluorescence (IF) and cell fractionation IB (Extended Data Fig. 2f, g). Using whole-cell lysates and membrane proteins of GSC23 cells, we validated 100% of the amino acids in MET404, including all four specific C-terminal a.a., by LC/MS (Extended Data Fig. 2h). To further confirm that MET404 was

generated from circMET instead of *MET* linear splicing variants, we used the CRISPR/Cas9 system to generate circMET knockout (KO) mice²³ (Fig. 2c). Deletion
135 of the downstream intron sequence of *mMET* exon 3 did not alter mMET mRNA expression (Extended Data Fig. 3a). However, CRISPR/Cas9-induced downstream intron element deletion repressed circularization efficiency and markedly inhibited circMET levels (Fig. 2d). Although circMET could not be completely deleted by this strategy, the markedly diminished MET404 expression and the un-affected MET
140 expression in multiple organs of circMET KO mice further indicated that circMET encoded this novel protein (Fig. 2e).

M⁶A modification and the YTHDF2 m⁶A reader are essential for circMET translation

CircMET is a m⁶A-modified, YTHDF2-associated circRNA, and YTHDF2 is a
145 validated glioma prognostic marker¹⁵. To investigate whether YTHDF2 is essential for circMET translation, we knocked down (KD) YTHDF2 in GSC456 and GSC23 cells. YTHDF2 KD did not affect circMET expression but reduced MET404 protein levels (Fig. 2f and Extended Data Fig. 3b). Meanwhile, the YTHDF2/circMET interaction was further investigated by IP (Fig. 2g). Interestingly, YTHDF1/3 KD did not affect
150 MET404 protein expression (Extended Data Fig. 3c, d). Overexpression (OE) of the m⁶A eraser ALKBH5 also reduced MET404 protein levels, while the ALKBH5 H204A mutant²⁴ did not (Extended Data Fig. 3e). The YTHDF2 mutants W432A and W486A²⁵ could not interact with circMET as YTHDF2 WT did and thus did not alter MET404 protein expression (Fig. 2h and Extended Data Fig. 3f). Inspection of several clinical

155 GBM samples and paired normal brain (NB) revealed that MET404 tended to be overexpressed in cancerous tissues (Fig. 2i, j). Notably, circMET and MET404 expression levels were markedly higher in GSCs than in NSCs or established GBM cell lines (Extended Data Fig. 1h and 3g). Accordingly, circMET and MET404 were also upregulated in CD133-positive cells compared with CD133-negative cells derived from
160 clinical surgical tumour samples (Extended Data Fig. 3h-k). In immunohistochemistry (IHC) of GBM samples, MET404 expression was spatially correlated with YTHDF2 expression (Fig. 2k), and high MET404 expression predicted worse overall survival of GBM patients (Fig. 2l).

165 ***MET404 promoted GBM tumorigenesis by activating MET signalling***

MET404 localized mainly on the cell membrane (Extended Data Fig. 2g). To explore the unknown function of MET404, we performed RNA-seq on GSC23 cells expressing circMET shRNA or scramble shRNA and on GSC28 cells overexpressing circMET RNA or empty vector. KEGG enrichment analysis was performed, and 31 pathways
170 were significantly enriched in both comparison groups, including several receptor tyrosine kinase (RTK)-related pathways and tumour-related pathways (Fig. 3a and Supp Table 5), implying that MET404 is involved in multiple cancerous signalling pathways. In GSC456 and GSC23 circMET stable KD cells, we examined several RTKs, including EGFR, PDGFR α , MET, FGFR, and TRKB, and found that only p-MET was markedly
175 inhibited (Fig. 3b and Extended Data Fig. 4a-b). In addition, p-MET downstream p-AKT(S473) activation was restrained. The cellular proliferation, limited dilution assays

and neurosphere formation ability assays revealed inhibition in both types of circMET KD GSCs (Fig. 3c-f and Extended Data Fig. 4c-e). OE of circMET RNA or MET404 ORF in GSC28 cells increased p-MET and p-AKT levels, as well as the
180 abovementioned biological functions (Extended Data Fig. 4f-l). OE of a mutant circMET RNA (insertion of an A to disrupt the MET404 ORF) did not achieve the same effects in GSC28 cells, suggesting that these effects were dependent on MET404 rather than circMET RNA (Extended Data Fig. 4f-l). In a mouse *in situ* tumorigenesis assay, KD MET404 inhibited mouse brain tumour xenograft growth and prolonged overall
185 survival (Fig. 3g, h and Extended Data Fig. 4m), while OE circMET RNA or MET404 ORF (but not circMET mut) further enhanced GBM progression (Extended Data Fig. 4n, o). Although homozygous MET KO mice could cause embryonic lethality²⁶, we did not observe abnormal phenotypes in circMET KO mice. This was probably because the intron KO reduced the circularization efficiency but did not completely abolish
190 MET404 expression and had no effect on MET expression. However, when challenging circMET KO mice with CCl₄²⁷, we found that the liver repair process was inhibited compared with that in WT mice (Fig. 3i, j). MET signalling intensity, which is critical for liver regeneration^{28,29}, was much lower in circMET KO mice than in WT mice (Fig. 3k and Extended Data Fig. 4p). Notably, CCl₄ treatment induced MET404 expression
195 within 6 hours, which suggested that MET404 is fast responded and critical for MET signalling (Fig. 3k).

A previous report showed that *P53*^{ff}; *PTEN*^{ff} mice developed spontaneous GBM³⁰. Given that MET404-activated p-AKT could mimic *PTEN*^{ff}, we generated *P53*^{ff}; *R26*-

MET404-flag^{LSL/+}; GFAP-Cre transgenic mice (MET404 KI mice, Fig. 4a-c). Most
200 MET404 KI mice developed brain tumours at 20 weeks (displayed central nervous
system symptoms including paralysis, seizure and/or ataxia), and the tumour
phenotypes were very similar to those of GBM, with highly activated MET signalling
(Fig. 4d, e). Compared with that in control mice (*P53^{ff}; R26-MET404-flag^{+/+}; GFAP-
Cre*, MST 48.35 weeks, often died due to mouse or subcutaneous tumours), the overall
205 survival was remarkably shorter in MET404 KI mice (MST 29.25 weeks, all died of
CNS tumours) (Fig. 4f). The above results suggested that MET404 is critical for GBM
tumorigenesis by activating MET signalling.

MET404 activates the MET receptor by interacting with the MET β subunit

210 We next explored the mechanism by which MET404 activates MET signalling.
Analysis of amino acid sequences strongly suggested that MET404 has a secretion
signal peptide (Extended Data Fig. 5a, b). Indeed, IB of the supernatant from GSCs
indicated that MET404 was secreted into the GSC culture medium (Fig. 5a). Purified
MET404 also activated MET and downstream signalling, and these effects could be
215 antagonized by the addition of a MET404 neutralization antibody (Fig. 5b, c and
Extended Data Fig. 5c). When MET receptor was stably KD in GSC28 and GSC387
cells, the activation of MET and downstream signalling induced by purified MET404
were inhibited (Fig. 5d). The above results suggested that MET404 exerted its effects
through the MET receptor.

220 We then performed MET404 immunoprecipitation-mass spectrometry (IP-MS) and

identified 196 candidate proteins as potential binding partners of MET404 (Supp Table 6). Enrichment analysis revealed several Gene Ontology (GO) terms related to extracellular localization and molecule binding (Fig. 5e), consistent with MET404's role as a secreted protein. Notably, MET was listed in the identified candidates (Fig. 5f and Extended Data Fig. 5d). Moreover, Reactome pathway analysis revealed that MET404-interacting proteins were highly associated with the RTK pathway, especially with MET signalling, including the regulation of MET activity, RAF/MAP kinase cascade, MAPK family signalling cascades, etc. (Fig. 5g and Supp Table 7). By utilizing the STRING database, a protein interaction network was established with MET as the hub based on the identified MET404 binding candidates (Fig. 5h), which included 3 direct binding partners of MET (RPS27A, HSP90AA1 and JAK1) and another 42 indirect interacting proteins. Next, we validated the MET404/MET interaction by mutual IP in GSC23 cells (Fig. 5i). Immunofluorescence (IF) also supported the conclusion that MET404 and MET colocalized in GSC23 and GSC456 cells, particularly on the cell membrane (Fig. 5j).

To elucidate MET404/MET receptor binding sites, we employed molecular docking (ClusPro server³¹) to simulate a complex formed from MET404 and MET ectodomain (Fig. 6a). The contact list of the final stable complex revealed that residues 542-650 (spanning the PSI and IPT1 domains of MET³²) on MET were key to mediating its interaction with MET404 (Fig. 6b, Supp Table 8). Inspired by the docking analysis, we synthesized constructs of the full-length MET receptor and several truncated MET receptor domains to identify the exact domain on MET that interacts with MET404.

Using eukaryotic purified MET404 and different MET truncations, we showed that MET404 interacted with the PSI+IPT1 domain of the MET receptor (Fig. 6c). In contrast, HGF interacted with the SEMA domain of the MET receptor³². Furthermore, we mutated several residues on MET404 that were predicted to have a strong interaction energy and found that a single mutation of D358 sufficiently abrogated the interaction, while a double mutation of Q328 and D358 completely abolished binding (Fig. 6d). Moreover, purified MET404 (1 $\mu\text{g}/\text{mL}$) treatment activated p-MET and downstream effectors earlier than HGF (100 ng/mL), and combination treatment with MET404/HGF showed a synergistic effect on p-MET activation (Fig. 6e, f).

Due to the different interaction region to MET receptor, we hypothesized that MET404 could independently activate p-MET without HGF. We generated HGF KO GSC23 and GSC456 cells (Extended Data Fig. 6a, b). In both HGF KO cell lines, slight p-MET downregulation was observed (Extended Data Fig. 6c), suggesting that HGF is responsible for part of the p-MET activity. Addition of purified MET404 boosted p-MET and downstream p-AKT signalling, indicating that MET404 alone could activate the MET receptor (Fig. 6g). We next generated MET404 KO GSC23 and GSC456 cells by abolishing circMET expression (Extended Data Fig. 6d). MET404 KO dramatically reduced p-MET levels in GSCs, indicating that MET404 is a major MET activator in GSCs (Extended Data Fig. 6c). Adding HGF to MET404 KO cells also increased p-MET and p-AKT levels, further suggesting that HGF and MET404 independently activate the MET receptor (Fig. 6h). Finally, we generated *MET* exon 2 KO GSCs (Extended Data Fig. 6e). Given that the MET receptor is formed by α and β subunits,

265 both of which are generated by cleavage of full-length MET³³, *MET* exon 2 KO
abolished both MET receptor and MET404 expression (Extended Data Fig. 6e, upper
right). Treatment with HGF or MET404 in *MET* exon 2 KO GSCs did not activate
downstream p-AKT (Fig. 6i). We then re-expressed the β subunits in these cells and
stimulated them with HGF or MET404. HGF stimulation could not activate p-MET and
270 p-AKT in these modified cells, supporting the conclusion that the α subunit is required
for the classic MET working model. In contrast, MET404 alone stimulated p-MET and
p-AKT in these modified cells, indicating that MET404 could form a complex with the
 β subunit and activate the MET receptor without HGF stimulation (Fig. 6i). Given the
aberrant expression of MET404, our data suggested that MET404 is the key activator
275 of hyperactivated MET signalling in GBM.

***Synergistic effects of targeting MET404 and onartuzumab in restraining GBM
progression***

In GBM clinical samples, we observed marked MET404 and p-MET colocalization
280 and observed that MET404 intensity correlated with p-MET levels (Fig. 7a).
Furthermore, MET404 expression was better correlated with p-MET levels in GBM
than with MET receptor expression and p-MET levels (Fig. 7b), supporting our
previous conclusion that MET404 is the major activator of p-MET in GBM. The dose-
dependent addition of MET-404 antibody gradually decreased p-MET in GSC23 and
285 GSC456 cells (Fig. 7c), implying the clinical potential of targeting MET404 in GBM.
Notably, the combination of MET404 and onartuzumab, an FDA-approved MET

signalling inhibitor which showed a negative effect in GBM clinical trials⁸, maximally inhibited MET signalling and downstream events including AKT activation and cellular viability (Fig. 7d). In mouse brain tumour xenografts, onartuzumab and MET404 antibody treatment achieved partial inhibition of MET phosphorylation and tumour progression; the combination of these two approaches, however, maximally inhibited GBM progression as well as *in vivo* MET signalling and prolonged the overall survival of experimental mice to more than 60 days (MST 56-59 days, Fig. 7e-g).

295 **Discussion**

Recent high-throughput m⁶A-seq data indicated that at least 13% of circRNAs carry the m⁶A modification¹⁴. M⁶A modification is sufficient to initiate circRNA translation with the initiation factor eIF4G2 and m⁶A reader proteins such as YTHDF3¹⁴. Given that YTHFD2 is a more highly expressed m⁶A reader than YTHFD3 in GBM¹⁵ and given their similar functions, it is reasonable to assume that YTHDF2 may drive aberrant circRNA translation in GBM. In this study, we showed that circMET is a highly expressed circRNA with intensive m⁶A modification in GBM and encodes MET404 in a YTHFD2-dependent manner. As epigenetic dysregulation is commonly seen in GBM^{24,34}, a considerable portion of circRNAs can generate unexpected molecular targets with better specificity than the current targets encoded by classic mRNAs. Large-scale screening for those targets is obviously needed in the future.

MET is one of the most significantly altered RTKs in GBM in addition to *EGFR* (approximately 4%)⁵. In addition, MET is detected in cancer-related endothelial cells,

which are critical for neoangiogenesis³⁵. To date, *MET* has been proven to be a
310 ‘signature gene’ in GBM that specifically contributes to the GBM mesenchymal
subtype³⁶. Although genetic amplification/mutation is relatively rare, the frequency of
MET expression in primary GBM varies from 30%-100%³⁷. With its single ligand, HGF
(also frequently overexpressed in GBM), HGF/MET signalling is a rational target for
GBM treatment. Nevertheless, neither HGF- nor MET-targeted therapy was proven
315 effective in current clinical trials^{8,38,39}. Here, we identified MET404 as a constitutive
ligand for the MET receptor. Together with the fact that MET404 is also overexpressed
in GBM and highly correlated with p-MET status, our results suggested that MET404
is an ideal target for MET-hyperactivated GBM, especially when used in combination
with other MET inhibitors (Fig. 7h). Given that MET activation/EGFR amplification is
320 usually mutually exclusive⁶, anti-EGFR therapy in these tumours is not mandatory; thus,
this approach could reduce side effects.

Overall, our work identified a novel molecular target, MET404, which is generated
by circMET, in GBM. As a previously unknown MET ligand, MET404 constitutively
activates the MET receptor and stimulates downstream effectors independent of HGF.

325

Materials and methods

Human glioma and paired adjacent normal tissues

All pathologically diagnosed glioma samples and adjacent normal brain tissues used in this study were collected from [REDACTED]

330 [REDACTED] with informed consent. The study was approved by [REDACTED]

[REDACTED] (Application ID: [2020]322).

Generation of transgenic mice based on CRISPR/Cas9 technology

C57BL/6 mice were used for the generation of transgenic mice. To generate circMET knockout mice, gRNAs targeting the intronic sequence of circMET (gRNA2: AAGACACGGAAGCTATTCTGTGG; gRNA3: TAGGCTTCTCGCTTAAAAGTTGG) and Cas9 mRNA were coinjected into fertilized mouse eggs to generate targeted knockout offspring. To generate MET404 knock-in (*R26-MET404-flag^{LSL/+}*) mice, the MET404-encoding sequence was cloned into a homologous recombination donor vector and then

340 coinjected with gRNA targeting the Rosa26 locus (gRNA: GGGGACACACTAAGGGAGCTTGG) and Cas9 mRNA into fertilized mouse eggs.

P53^{ff} mice were generated using a standard knock-in approach in which *P53* exons 5-7 were flanked by loxP sites. GFAP-Cre mice, *P53^{ff}* mice and *R26-MET404-flag^{LSL/+}* mice were hybridized to generate control (*P53^{ff}; R26-MET404-flag^{+/+}; GFAP-Cre*)

345 mice and MET404 KI (*P53^{ff}; R26-MET404-flag^{LSL/+}; GFAP-Cre*) mice. Gene-targeted mice were identified by PCR screening and DNA sequencing. All experimental

protocols concerning the handling of mice were approved by [REDACTED]
[REDACTED] (Application No. [2021]059). All mice were housed, bred, and maintained under specific pathogen-free (SPF) conditions.

350 *Xenograft studies*

Four-week-old female BALB/c-nu mice were purchased from the Laboratory Animal Centre of [REDACTED]. The mice were housed in a temperature-controlled (22 °C) and light-controlled specific pathogen-free animal facility with free access to food and water. All experimental protocols concerning the handling of mice were
355 approved by [REDACTED]
[REDACTED] (Application No. [2021]059).

Each group contained five mice. Mice were injected with 5000 of the indicated cells intracranially. For the drug treatment experiments, 10 days after the initial tumour implantation, mice were injected intracranially with IgG (3 µg), anti-MET404
360 monoclonal antibody (3 µg), onartuzumab (3 µg) or anti-MET404 combined with onartuzumab (3 µg each) through a screw guide (Protech International) every 3 days.

When the first mouse showed neurologic symptoms that significantly affected their quality of life (such as seizures, ataxia and lethargy, inability to feed), all the mice were sacrificed, and their brains were harvested, fixed in 4% formaldehyde, embedded in
365 paraffin and then subjected to haematoxylin and eosin staining and IHC staining. For the survival experiments, all the mice were monitored until they showed severe neurologic symptoms and had to be sacrificed humanely. The overall survival curves were calculated with the Kaplan–Meier method and compared by the log-rank test.

Acute liver injury model

370 This model was established closely following methods previously reported^{29,40}. In brief, 8- to 12-week-old male wild-type and circMET KO mice (C57/BL6J background) received one intraperitoneal injection of 1 mL/kg CCl₄ (Macklin #56-23-5, diluted in mineral oil (Sigma, #M5310) at a ratio of 1 to 4). For uninjured controls, 1 mL/kg filtered mineral oil was administered. After 6 and 24 hours, the liver was collected for
375 further immunoblot analysis. On days 1, 2, 3, 5 and 7, the liver tissue was collected and fixed in 4% paraformaldehyde (PFA), embedded in paraffin and stained with haematoxylin and eosin.

Cell culture studies

GSCs, including 387, 456, 28, and 23, were kindly provided by Dr. Jeremy Rich,
380 UPMC. These cells were cultured in DMEM/F12 medium (Gibco) supplemented with B27 supplement (Life Technologies), bFGF and EGF (20 ng m l⁻¹ each, R&D systems). 293T (CRL-11268) and U118 (HTB-15) cells were purchased from ATCC. U251 and SNB19 cells were kindly provided by Dr. Suyun Huang, VCU. These cell lines were cultured in Dulbecco's modified Eagle's medium (Gibco) supplemented with 10%
385 foetal bovine serum (Gibco) according to standard protocols. NHA cells were purchased from Lonza and cultured using an AGMTM Astrocyte Growth Medium Bullet KitTM (Lonza), as recommended by the manufacturer. Primary human NSCs were obtained from Thermo Fisher (A15654) and Gibco (TM A15654) , and cultured with StemPro NSC SFM (A10509-01) supplemented with 2 mM GlutaMAX-I supplement
390 (35050), 6 U ml⁻¹ heparin (Sigma, H3149) and 200 μM ascorbic acid (Sigma, A8960).

All cells used in this study were cultured in a humidified incubator at 37 °C with 5% CO₂ and were free of mycoplasma contamination (regularly tested).

Constructs and reagents

The pEZ-ALKBH5 WT and pEZ-ALKBH5 mutant (H204A) plasmids were kind
395 gifts from Dr. Shirong Cai (First Affiliated Hospital of Sun Yat-sen University, China).
The YTHDF2 WT, W432A mutant and W486A mutant plasmids were kindly provided
by Prof. Xiuxing Wang (Nanjing Medical University, China). The circMET
overexpression plasmid, circMET Mut and circMET ORF plasmids, and His-MET404
plasmid were generated by chemical gene synthesis, and the pCDH-CMV-MCS-EF1-
400 copGFP-T2A-Puro vector was used as the plasmid backbone (Generay Biotech, China).
Flag-tagged full-length and truncated MET overexpression plasmids were generated by
chemical gene synthesis and inserted into the pcDNA 3.1(+) construct (Generay
Biotech, China). All the siRNAs and shRNAs in this paper were generated by
GenePharma, China. The target sequences are listed in Supp Table 9. Recombinant
405 human HGF (Z03229) was purchased from GeneScript, China. Onartuzumab
(ATAD00251) was generated by AtaGenix, China.

N⁶-methyladenosine immunoprecipitation (m⁶A IP) and sequencing

After total RNA was extracted, the enriched RNA was broken into short fragments
(approximately 100 nt) by using fragmentation buffer. The RNA was divided into two
410 parts, one of which was used as the input (no IP experiment was performed). The other
portion of the RNA was enriched with an m⁶A-specific antibody. The input and enriched

RNA were reverse transcribed into cDNA with random primers. Next, the cDNA fragments were end repaired and ligated to Illumina sequencing adapters. The quality-tested library was sequenced using an Illumina NovaSeq™ 6000 by Gene Denovo
415 Biotechnology Co. (Guangzhou, China).

Raw reads obtained from the sequencing machines were processed using fastp⁴¹ (version: 0.20.0) software to obtain high-quality clean reads. The short read alignment tool Bowtie2⁴² (version 2.2.8) was used for mapping reads to the ribosome RNA (rRNA) database. The rRNA mapped reads were removed. The remaining reads were further
420 used in alignment and analysis. The rRNA-removed reads from each sample were then mapped to the reference genome by HISAT2⁴³ (version 2.1.1). After alignment with the reference genome, the reads that could be mapped to the genomes were discarded, and the unmapped reads were then collected for circRNA identification. Twentymers from both ends of the unmapped reads were extracted and aligned to the reference genome
425 to find unique anchor positions within the splice site. Anchor reads that aligned in the reverse orientation (head-to tail) indicated circRNA splicing and were subjected to find_circ⁴⁴ to identify circRNAs. The anchor alignments were then extended such that the complete read aligns and the breakpoints were flanked by GU/AG splice sites. A candidate circRNA was called if it was supported by at least two unique back-spliced
430 reads in at least one sample. CircRNAs were blasted against circBase⁴⁵ for annotation. Those that could not be annotated were defined as novel circRNAs. The source gene is the origin gene of a circRNA. We performed KEGG⁴⁶ enrichment analysis of source genes to study the main functions of these source genes of circRNAs.

Ribosome-nascent chain complex (RNC) sequencing and bioinformatics analysis

435 RNC-seq was performed as described previously¹⁷. Briefly, cells were pretreated with 100 µg/ml cycloheximide for 15 min before lysis. Cell lysates were transferred onto the surface of 30% sucrose RB buffer and then subjected to ultracentrifugation at 185,000 × g for 5 h at 4 °C for RNC precipitation. RNA in total cell lysates and RNC-mRNAs was extracted and subjected to RNA sequencing. RNC-RNA was extracted
440 using a TRIzol reagent kit (Invitrogen, Carlsbad, CA, USA) according to the manufacturer's protocol. RNA quality was assessed on an Agilent 2100 Bioanalyzer (Agilent Technologies, Palo Alto, CA, USA) and checked using RNase-free agarose gel electrophoresis. After RNC-RNA was extracted, rRNAs were removed to retain mRNAs and ncRNAs. The enriched mRNAs and ncRNAs were broken into short
445 fragments by using fragmentation buffer and reverse transcribed into cDNA with random primers. Second-strand cDNA was synthesized with DNA polymerase I, RNase H, dNTPs (dUTP instead of dTTP) and buffer. Next, the cDNA fragments were purified with a QiaQuick PCR extraction kit (Qiagen, Venlo, The Netherlands), end repaired, poly(A) conjugated, and ligated to Illumina sequencing adapters. Then, uracil-N-
450 glycosylase (UNG) was used to digest the second-strand cDNA. The digested products were size selected by agarose gel electrophoresis, PCR amplified, and sequenced using an Illumina NovaSeq™ 6000 by Gene Denovo Biotechnology Co. (Guangzhou, China).

The method of circRNA detection for RNC-seq data was the same as that used for
455 m⁶A -seq. To quantify circRNAs, back-spliced junction reads were scaled to RPM

(reads per million mapped reads). To identify differentially expressed circRNAs across samples or groups, the edgeR package⁴⁷ (version 3.12.1) (<http://www.r-project.org/>) was used. We identified circRNAs with a fold change ≥ 2 and a P value ≤ 0.05 .

N⁶-methyladenosine immunoprecipitation (m⁶A IP) and RT-qPCR analysis

460 M⁶A IP was conducted using a Methylated RNA Immunoprecipitation Kit (BersinBio, Bes5203) according to the manufacturer's instructions. Briefly, 1×10^7 cells were prepared and subjected to RNA extraction using TRIzol Reagent (Invitrogen). Immunoprecipitation was performed using an anti-m⁶A antibody (Synaptic Systems, 202003) and protein A/G beads. RNAs from the eluate (m⁶A positive) and supernatant
465 (m⁶A negative) were purified separately and subjected to RT-qPCR analysis.

RNA-Binding Protein Immunoprecipitation Assay (RIP) and sequencing

The RIP assay was performed as previously described, with minor modifications⁴⁸. Briefly, 5 μ g anti-YTHDF2 antibody (Proteintech, 24744-1-AP) was precoated onto protein A/G beads at 4 °C overnight. The cell pellet was lysed using ice-cold polysome
470 extraction buffer supplemented with RNase inhibitors and protease inhibitors. For each RIP, 1000 μ g lysate was incubated with precoated beads for 1.5 h at 4 °C with rotation. After incubation, the beads were washed 5 times and subjected to DNA and protein digestion and RNA extraction. The isolated RNA was then subjected to sequencing and RT-qPCR analysis. For sequencing analysis, the input and YTHDF2-antibody-enriched
475 RNA was broken into short fragments (approximately 250 nt) by using fragmentation buffer and then reverse-transcribed into cDNA with random primers. Next, the cDNA

fragments were end repaired and ligated to Illumina sequencing adapters. The quality-tested library was sequenced using an Illumina NovaSeq™ 6000 by Gene Denovo Biotechnology Co. (Guangzhou, China). The method of circRNA detection used for the
480 YTHDF2 RIP-seq data was the same as that used for the m⁶A-seq data.

RT-qPCR analysis

PrimeScript™ RT Master Mix (Takara) was used according to the manufacturer's instructions for RNA reverse transcription unless otherwise indicated. Quantitative polymerase chain reaction (qPCR) was performed using TB Green® Premix Ex Taq™
485 II (Tli RNaseH Plus) (Takara). The primer sequences are listed in Supp Table 9. The relative expression levels were calculated according to $2^{-\Delta\Delta CT}$.

RNase-R treatment

Total RNA was extracted and then treated with RNase-R (Lucigen) at 37 °C for 15 min. The RNase-R resistance of circMET was evaluated by RT-qPCR analysis.

Actinomycin D assay

293T cells were treated with actinomycin D (2 µg/ml, HY-17559, MedChem Express) for 0 h, 4 h, 8 h, 12 h and 24 h. Then, the cells were harvested at the indicated timepoints, and the relative RNA levels of circMET and linear-MET were analysed by RT-qPCR and normalized to the values obtained in the 0 h group.

RNA fluorescence in situ hybridization (FISH)

Cy3-labelled oligonucleotide probes complementary to the circMET junction region were designed using the Clone Manager suite of analysis tools (Sci Ed Central, listed

in Supp Table 9). The indicated cells were precoated with poly-L-ornithine and laminin (Sigma) on a cover glass-bottom confocal dish and cultured overnight. FISH assays were performed using an RNA FISH kit (GenePharma, China) according to the manufacturer's instructions. Nuclei were stained with 4,6-diamidino-2-phenylindole (DAPI). Images were acquired on a ZEISS LSM 880 with Airyscan.

RNA subcellular isolation

Cytoplasmic and nuclear fractions were isolated using the reagents supplied in the RNA subcellular isolation kit (Active Motif). Briefly, cells were lysed in complete lysis buffer and incubated for 10 minutes on ice. After centrifugation, the supernatant was transferred for cytoplasmic RNA extraction, and the remaining pellet was collected for nuclear RNA purification. RNA products were subjected to RT-qPCR analysis.

Polysome profiling assay

The details of the polysome profiling analysis were described previously⁴⁹. Briefly, 1×10^7 cells were treated with 100 $\mu\text{g}/\text{mL}$ cycloheximide in DMSO for 5 min at 37 °C and then harvested for polysome profiling. Cells were lysed in 500 μl polysome lysis buffer, followed by centrifugation. The supernatant was then loaded onto a 5-50% (w/v) sucrose density gradient, ultracentrifuged at 20,000 \times g for 2 h at 4 °C in a Beckman SW41 rotor and subsequently fractionated using a BioComp PGFip Piston Gradient Fractionator Model 152. The absorbance at 254 nm was measured using an absorbance detector connected to the fraction collector. RNA was extracted from different fractions, and RT-qPCR was conducted to evaluate the distribution of targets.

Immunoblotting

520 Briefly, after extraction with RIPA buffer supplemented with protease inhibitor and
phosphatase inhibitor cocktails (MedChem Express) and quantification with a BCA kit
(Thermo Fisher), equal amounts of protein from cell lysates or tissue lysates were
denatured by boiling, resolved by SDS–polyacrylamide gels and transferred to
polyvinylidene fluoride (PVDF) membranes. After blocking with 5% nonfat milk, the
525 membranes were consecutively incubated with the indicated primary antibodies and
HRP-conjugated secondary antibodies (Invitrogen). The chemiluminescence signals
were detected using Clarity™ Western ECL Substrate (Bio–Rad). The anti-MET404
mouse monoclonal antibody was generated by GenScript, China. Other primary
antibodies are listed below: anti-ALKBH5 (Proteintech, 16837-1-AP); anti-YTHDF2
530 (Proteintech, 24744-1-AP); anti-YTHDF1 (Proteintech, 17479-1-AP); anti-YTHDF3
(Proteintech, 25537-1-AP); anti-P53 (Proteintech, 60283-2-Ig); anti-MET (Abcam,
ab51067); anti-MET (Cell Signaling Technology, 8198), anti-phospho-MET
Tyr1234/1235 (Cell Signaling Technology, 3077); anti-AKT (Cell Signaling
Technology, 4691); anti-phospho-AKT Ser473 (Cell Signaling Technology, 4060), anti-
535 6x-His tag (Abcam, ab18184), anti-EGFR (Boster, A0023), anti-phospho EGFR Y1068
(Abcam, ab40815), anti-PDGFR A (Abcam, ab248689), anti-phospho PDGFRA Y720
(Abcam, ab134068), anti-FGFR1 (Abcam, ab76464), anti-phospho FGFR1 Y654
(Abcam, ab59194), anti-pan TRK (Abcam, ab76291), anti-phospho TRKB Y705
(Abcam, ab229908), anti-6x-His tag antibody (Abcam, 18184), anti-flag tag antibody

540 (F1804, Sigma-Aldrich), anti- β -actin (A1978, Sigma-Aldrich), and anti- β -tubulin (Cell Signaling Technology, 2128).

Processing of human glioma tissue and CD133⁺ cell isolation

Fresh human glioma tissue was minced, digested (collagenase IV (1 mg/ml, Gibco), DNase I (20 U/ml, Sigma–Aldrich), hyaluronidase (0.01%, Solarbio) and DMEM/F12
545 (Gibco)) for 40 minutes at 37 °C, and sequentially filtered through 70- μ m and 40- μ m strainers. Myelin was removed by Debris Removal Solution (130-109-398, Miltenyi Biotec) according to the manufacturer’s instructions. Red blood cells were then lysed with RBC lysis buffer (C3702, Beyotime). Next, the collected cell pellet was resuspended in FACS staining buffer (PBS containing 2% FBS) and stained with anti-
550 CD133 PE (566593, BD Biosciences). Homologous IgG was used as an isotype control antibody. Fixable Viability Dye eFluor 520 (65-0867-14, eBioscience) was applied to rule out dead cells. Live CD133-positive and CD133-negative cells were sorted on a BD FACSAria II Cell Sorter. The collected cells were then subjected to RNA or protein extraction before qPCR or immunoblot analysis.

555 ***LC–MS analysis***

Proteins were separated via SDS-PAGE and subjected to digestion. Chymotrypsin was used to analyse the specific tail of MET404. Otherwise, trypsin was used for digestion. The digested peptides were analysed with a QExactive mass spectrometer (Thermo Fisher). The fragment spectra were analysed using the National Centre for
560 Biotechnology Information nonredundant protein database with Mascot. For LC/MS

analysis of membrane proteins, a Membrane and Cytosol Protein Extraction Kit (Beyotime, P0033) was used to extract membrane proteins from the indicated cells. GO enrichment (<http://www.geneontology.org/>) and Reactome enrichment (<https://reactome.org/>) were conducted for the proteins detected from Met404 Co-IP.

565 The protein interaction network was generated using the string database (<https://cn.string-db.org/>). The network around MET was plotted using Cytoscape⁵⁰.

Immunoprecipitation (IP)

Cells were lysed in co-IP soft RIPA Lysis Buffer (Beyotime, China) supplemented with protease and phosphatase inhibitors. The supernatant was collected and subjected
570 to immunoprecipitation using the indicated primary antibodies at 4 °C overnight. Then, the lysates were incubated with 30 µL protein A/G agarose (Gibco) for 2 h at room temperature. The collected agarose-protein complexes were centrifuged and washed with cold PBST (PBS containing 0.1% Tween 20) for 5 times and then subjected to SDS-PAGE and analysed by LC-MS or immunoblotting.

575 ***Immunofluorescence (IF) staining***

Seeded cells on coverslips or frozen glioblastoma sections were fixed with 4% paraformaldehyde for 15 min, permeabilized with PBS containing 0.1% Triton X-100 for 5 min at room temperature, blocked with 5% BSA in PBS, and then incubated with an anti-MET404 monoclonal antibody (generated by GeneScript, China), anti-MET
580 antibody (Abcam, ab51067) anti-phospho-MET Tyr1234/1235 (Cell Signaling Technology, 3077) overnight at 4 °C, followed by the appropriate secondary

fluorescently labelled antibodies (Invitrogen) for one hour at room temperature. Nuclei were counterstained with DAPI. Images were acquired using a ZEISS LSM 880 with Airyscan.

585 ***Immunohistochemistry (IHC)***

Paraffin-embedded brain tissues were sectioned at a 4-mm thickness. Xylene and ethanol at a gradient of concentrations were used for dewaxing and hydration. Antigen retrieval was performed using a microwave for 20 minutes in 0.01 M citrate buffer (pH 6.0). After blocking with 3% H₂O₂ and then 10% FBS, the samples were incubated with
590 primary antibody overnight at 4 °C and secondary antibody for 30 min at room temperature. Immunodetection was performed using DAB solution. Tissues were counterstained with haematoxylin. The primary antibodies used in this paper are listed below: anti-MET404 monoclonal antibody (generated by GeneScript, China); anti-YTHDF2 (Proteintech, 24744-1-AP); anti-GFAP (Abcam, ab7260); anti-Nestin
595 (Abcam, ab221660); anti-Ki67 (Abcam, ab15580); and anti-phospho-MET (Cell Signaling Technology, 3077).

Molecular docking

Protein–protein docking in the ClusPro server⁵¹ was used for molecular docking simulations for complexes MET with MET404. The crystal structure for MET was
600 downloaded from the RCSB Protein Data Bank (PDB ID: 2UZY). For protein docking, the smaller protein (a smaller number of residues) is usually set as the ligand and the other as the receptor. The ligand was subjected to 70,000 rotations. For each rotation,

the ligand was translated along the x, y, and z axes relative to the receptor on a grid. One translation with the best score was chosen from each rotation. Of the 70,000
605 rotations, the 1000 rotation/translation combinations with the lowest score were chosen. Then, greedy clustering of these 1000 ligand positions with a 9 Å C-alpha RMSD radius was performed to find the ligand positions with the most “neighbours” at 9 Å, i.e., cluster centres. The top ten cluster centres with the most cluster members were then retrieved, and the intermolecular contacts from the most likely pose were further
610 evaluated.

Proliferation assay

Cell proliferation experiments were conducted by seeding cells of interest at a density of 2000 cells per well into 96-well plates. At the indicated time points, cell viability was determined using a Cell Counting Kit-8 (Dojindo). All data were normalized to day 1
615 and presented as the mean±SD. All experiments were performed in triplicate.

Neurosphere formation assay

Briefly, decreasing numbers of cells per well (20, 10, 5, 2 and 1) were plated into 96-well plates. The presence of neurospheres in each well was recorded seven days after plating. Extreme limiting dilution analysis was performed using software available
620 online (<http://bioinf.wehi.edu.au/software/elda>). All experiments were performed in triplicate.

EdU incorporation assay

The indicated cells were seeded on precoated coverslips, and EdU incorporation rates
625 were determined by a BeyoClick™ EdU Cell Proliferation Kit with Alexa Fluor 594
(Beyotime, China) according to the manufacturer's instructions. All experiments were
performed in triplicate.

Statistical analysis

Statistical tests were conducted using GraphPad Prism (Version 8; La Jolla) software
630 unless otherwise indicated. The data are presented as the mean \pm standard deviation
(S.D.) from three independent experiments. For the comparison of parametric data
between glioma samples and adjacent normal brain tissues, paired two-tailed Student's
t tests were used. For other parametric data, unpaired two-tailed Student's t tests or one-
way ANOVA were used. Overall survival curves were assessed with the Kaplan–Meier
635 method and compared by the log-rank test. The correlations were calculated by Pearson
correlation analysis. The data distribution was assumed to be normal, but this was not
formally tested. A level of $P < 0.05$ was used as the cut-off for significant differences.
For each experiment, the data are representative of three replicates, and similar results
were obtained.

Data availability

The sequencing data have been deposited in the National Genomics Data Centre
(GSA database, <https://ngdc.cnca.ac.cn/>) under the accession code PRJCA005969.

Acknowledgment

645 We gratefully thank all patients who participated in these studies. [REDACTED]

[REDACTED]

[REDACTED]

[REDACTED]

[REDACTED]

650

Competing interests

The authors declare no competing interests.

Author contributions

655 [REDACTED]

[REDACTED]

[REDACTED]

[REDACTED]

660 **Reference**

1. Tan, A. C. *et al.* Management of glioblastoma: State of the art and future directions. *CA. Cancer J. Clin.* **70**, 299–312 (2020).
2. Gilbert, M. R. *et al.* A randomized trial of bevacizumab for newly diagnosed glioblastoma. *N. Engl. J. Med.* **370**, 699–708 (2014).
- 665 3. Wick, W. *et al.* Lomustine and Bevacizumab in Progressive Glioblastoma. *N. Engl. J. Med.* **377**, 1954–1963 (2017).
4. Lim, M., Xia, Y., Bettgowda, C. & Weller, M. Current state of immunotherapy for glioblastoma. *Nat. Rev. Clin. Oncol.* **15**, 422–442 (2018).
5. The Cancer Genome Atlas Research Network. Comprehensive genomic characterization defines human glioblastoma genes and core pathways. *Nature* **455**, 1061–1068 (2008).
- 670 6. Snuderl, M. *et al.* Mosaic amplification of multiple receptor tyrosine kinase genes in glioblastoma. *Cancer Cell* **20**, 810–817 (2011).
7. Hu, H. *et al.* Mutational Landscape of Secondary Glioblastoma Guides MET-Targeted Trial in Brain Tumor. *Cell* **175**, (2018).
- 675 8. Cloughesy, T. *et al.* Randomized, Double-Blind, Placebo-Controlled, Multicenter Phase II Study of Onartuzumab Plus Bevacizumab Versus Placebo Plus Bevacizumab in Patients With Recurrent Glioblastoma: Efficacy, Safety, and Hepatocyte Growth Factor and O-Methylguanine-DNA Methyltransferase Biomarker Analyses. *J. Clin. Oncol. Off. J. Am. Soc. Clin. Oncol.* **35**, 343–351 (2017).
9. Gao, X. *et al.* Circular RNA-encoded oncogenic E-cadherin variant promotes glioblastoma tumorigenicity through activation of EGFR–STAT3 signalling. *Nat. Cell Biol.* (2021) doi:10.1038/s41556-021-00639-4.
10. Wu, X. *et al.* A novel protein encoded by circular SMO RNA is essential for Hedgehog signaling activation and glioblastoma tumorigenicity. *Genome Biol.* **22**, 33 (2021).
- 685 11. Liang, W.-C. *et al.* Translation of the circular RNA circ β -catenin promotes liver cancer cell growth through activation of the Wnt pathway. *Genome Biol.* **20**, 84 (2019).
12. Li, Y. *et al.* HNRNPL Circularizes ARHGAP35 to Produce an Oncogenic Protein. *Adv. Sci.* 2001701 (2021) doi:10.1002/advs.202001701.
- 690 13. Gu, C. *et al.* circGprc5a Promoted Bladder Oncogenesis and Metastasis through Gprc5a-Targeting Peptide. *Mol. Ther. - Nucleic Acids* **13**, 633–641 (2018).
14. Yang, Y. *et al.* Extensive translation of circular RNAs driven by N6-methyladenosine. *Cell Res.* **27**, 626–641 (2017).
- 695 15. Dixit, D. *et al.* The RNA m6A reader YTHDF2 maintains oncogene expression and is a targetable dependency in glioblastoma stem cells. *Cancer Discov.* CD-20-0331 (2020) doi:10.1158/2159-8290.CD-20-0331.
16. Zhang, L. *et al.* The role of N6-methyladenosine (m6A) modification in the

- regulation of circRNAs. *Mol. Cancer* **19**, 105 (2020).
- 700 17. Zhang, M. *et al.* A peptide encoded by circular form of LINC-PINT suppresses oncogenic transcriptional elongation in glioblastoma. *Nat. Commun.* **9**, 4475 (2018).
18. van Heesch, S. *et al.* The Translational Landscape of the Human Heart. *Cell* **178**, 242-260.e29 (2019).
19. Wang, X. *et al.* N6-methyladenosine Modulates Messenger RNA Translation Efficiency. *Cell* **161**, 1388–1399 (2015).
- 705 20. Karamouzis, M. V., Konstantinopoulos, P. A. & Papavassiliou, A. G. Targeting MET as a strategy to overcome crosstalk-related resistance to EGFR inhibitors. *Lancet Oncol.* **10**, 709–717 (2009).
21. De Bacco, F. *et al.* MET inhibition overcomes radiation resistance of glioblastoma stem-like cells. *EMBO Mol. Med.* **8**, 550–568 (2016).
- 710 22. Huang, W. *et al.* TransCirc: an interactive database for translatable circular RNAs based on multi-omics evidence. *Nucleic Acids Res.* **49**, D236–D242 (2021).
23. Zhu, P. *et al.* IL-13 secreted by ILC2s promotes the self-renewal of intestinal stem cells through circular RNA circPan3. *Nat. Immunol.* **20**, 183–194 (2019).
- 715 24. Zhang, S. *et al.* m6A Demethylase ALKBH5 Maintains Tumorigenicity of Glioblastoma Stem-like Cells by Sustaining FOXM1 Expression and Cell Proliferation Program. *Cancer Cell* **31**, 591-606.e6 (2017).
25. Zhu, T. *et al.* Crystal structure of the YTH domain of YTHDF2 reveals mechanism for recognition of N6-methyladenosine. *Cell Res.* **24**, 1493–1496 (2014).
- 720 26. Bladt, F., Riethmacher, D., Isenmann, S., Aguzzi, A. & Birchmeier, C. Essential role for the c-met receptor in the migration of myogenic precursor cells into the limb bud. *Nature* **376**, 768–771 (1995).
27. Zhao, L. *et al.* Tissue Repair in the Mouse Liver Following Acute Carbon Tetrachloride Depends on Injury-Induced Wnt/ β -Catenin Signaling. *Hepatology* hep.30563 (2019) doi:10.1002/hep.30563.
- 725 28. Borowiak, M. *et al.* Met provides essential signals for liver regeneration. *Proc. Natl. Acad. Sci. U. S. A.* **101**, 10608–10613 (2004).
29. Ishikawa, T. *et al.* Hepatocyte growth factor/c-met signaling is required for stem-cell-mediated liver regeneration in mice. *Hepatology* **55**, 1215–1226 (2012).
- 730 30. Zheng, H. *et al.* p53 and Pten control neural and glioma stem/progenitor cell renewal and differentiation. *Nature* **455**, 1129–1133 (2008).
31. Comeau, S. R., Gatchell, D. W., Vajda, S. & Camacho, C. J. ClusPro: a fully automated algorithm for protein-protein docking. *Nucleic Acids Res.* **32**, W96-99 (2004).
- 735 32. Uchikawa, E., Chen, Z., Xiao, G.-Y., Zhang, X. & Bai, X. Structural basis of the activation of c-MET receptor. *Nat. Commun.* **12**, 4074 (2021).
33. Giordano, S. *et al.* Biosynthesis of the protein encoded by the c-met proto-oncogene. *Oncogene* **4**, 1383–1388 (1989).

- 740 34. Chaligne, R. *et al.* Epigenetic encoding, heritability and plasticity of glioma transcriptional cell states. *Nat. Genet.* **53**, 1469–1479 (2021).
35. Abounader, R. & Lattera, J. Scatter factor/hepatocyte growth factor in brain tumor growth and angiogenesis. *Neuro-Oncol.* **7**, 436–451 (2005).
36. Behnan, J., Finocchiaro, G. & Hanna, G. The landscape of the mesenchymal signature in brain tumours. *Brain J. Neurol.* **142**, 847–866 (2019).
- 745 37. Boccaccio, C. & Comoglio, P. M. The MET Oncogene in Glioblastoma Stem Cells: Implications as a Diagnostic Marker and a Therapeutic Target. *Cancer Res.* **73**, 3193–3199 (2013).
38. Affronti, M. L. *et al.* Phase II Study to Evaluate the Efficacy and Safety of Rilotumumab and Bevacizumab in Subjects with Recurrent Malignant Glioma. *The oncologist* **23**, 889-e98 (2018).
- 750 39. Cloughesy, T. F. *et al.* Phase II study of cabozantinib in patients with progressive glioblastoma: subset analysis of patients with prior antiangiogenic therapy. *Neuro-Oncol.* **20**, 259–267 (2018).
40. Scholten, D., Trebicka, J., Liedtke, C. & Weiskirchen, R. The carbon tetrachloride model in mice. *Lab. Anim.* **49**, 4–11 (2015).
- 755 41. Chen, S., Zhou, Y., Chen, Y. & Gu, J. fastp: an ultra-fast all-in-one FASTQ preprocessor. *Bioinforma. Oxf. Engl.* **34**, i884–i890 (2018).
42. Langmead, B. & Salzberg, S. L. Fast gapped-read alignment with Bowtie 2. *Nat. Methods* **9**, 357–359 (2012).
- 760 43. Kim, D., Langmead, B. & Salzberg, S. L. HISAT: a fast spliced aligner with low memory requirements. *Nat. Methods* **12**, 357–360 (2015).
44. Memczak, S. *et al.* Circular RNAs are a large class of animal RNAs with regulatory potency. *Nature* **495**, 333–338 (2013).
45. Glažar, P., Papavasileiou, P. & Rajewsky, N. circBase: a database for circular RNAs. *RNA N. Y. N* **20**, 1666–1670 (2014).
- 765 46. Kanehisa, M. *et al.* KEGG for linking genomes to life and the environment. *Nucleic Acids Res.* **36**, D480-484 (2008).
47. Robinson, M. D., McCarthy, D. J. & Smyth, G. K. edgeR: a Bioconductor package for differential expression analysis of digital gene expression data. *Bioinforma. Oxf. Engl.* **26**, 139–140 (2010).
- 770 48. Martindale, J. L., Gorospe, M. & Idda, M. L. Ribonucleoprotein Immunoprecipitation (RIP) Analysis. *Bio-Protoc.* **10**, e3488 (2020).
49. AU - Gandin, V. *et al.* Polysome Fractionation and Analysis of Mammalian Translatomes on a Genome-wide Scale. *J. Vis. Exp.* e51455 (2014) doi:10.3791/51455.
- 775 50. Shannon, P. *et al.* Cytoscape: a software environment for integrated models of biomolecular interaction networks. *Genome Res.* **13**, 2498–2504 (2003).
51. Kozakov, D. *et al.* The ClusPro web server for protein-protein docking. *Nat. Protoc.* **12**, 255–278 (2017).

Figures

780 **Figure 1**

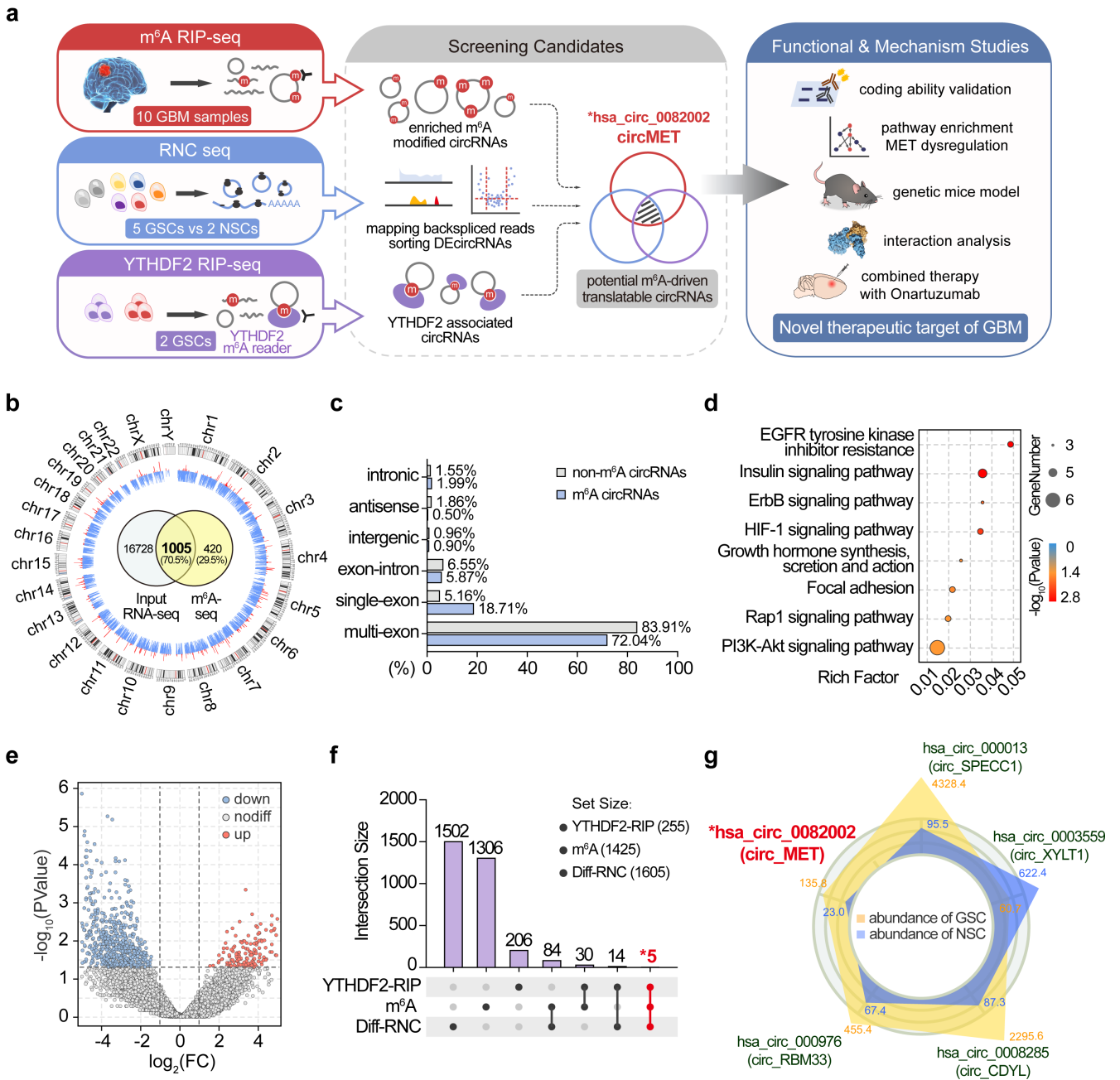


Figure 1. CircMET is a potential coding circRNA subjected to m⁶A modification

- 785 a. Experimental strategy. GSC, glioma stem cell. NSC, neural stem cell. DEcircRNAs, differentially expressed circRNAs.
- b. The circos plot shows the genome-wide m⁶A-modified circRNAs in GBM tissues. The outer circle represents the karyotype and centromere of chromosomes. The height of blue and red ticks represents the number of circRNAs detected (1~10) in input RNA-seq or m⁶A-seq, respectively. The Venn diagram in the centre illustrates the exact number of circRNAs detected in the m⁶A -seq and RNA-seq input data.
- 790 c. Comparison of the source regions of m⁶A circRNAs and non m⁶A circRNAs.
- d. KEGG enrichment analysis of the source genes of m⁶A circRNAs.
- e. Volcano plot showing differentially expressed circRNAs between GSCs and NSCs in the RNC-seq data.
- 795 f. Upset plot illustrating the number of circRNAs detected by m⁶A -seq, RNC-seq and YTHDF2 RIP-seq.
- g. Five candidate circRNAs were screened from the overlap of the m⁶A -seq, RNC-seq and YTHDF2 RIP-seq data. The yellow and blue polygons represent the RNC-seq expression levels of circRNAs in GSCs and NSCs, respectively.
- 800

Figure 2

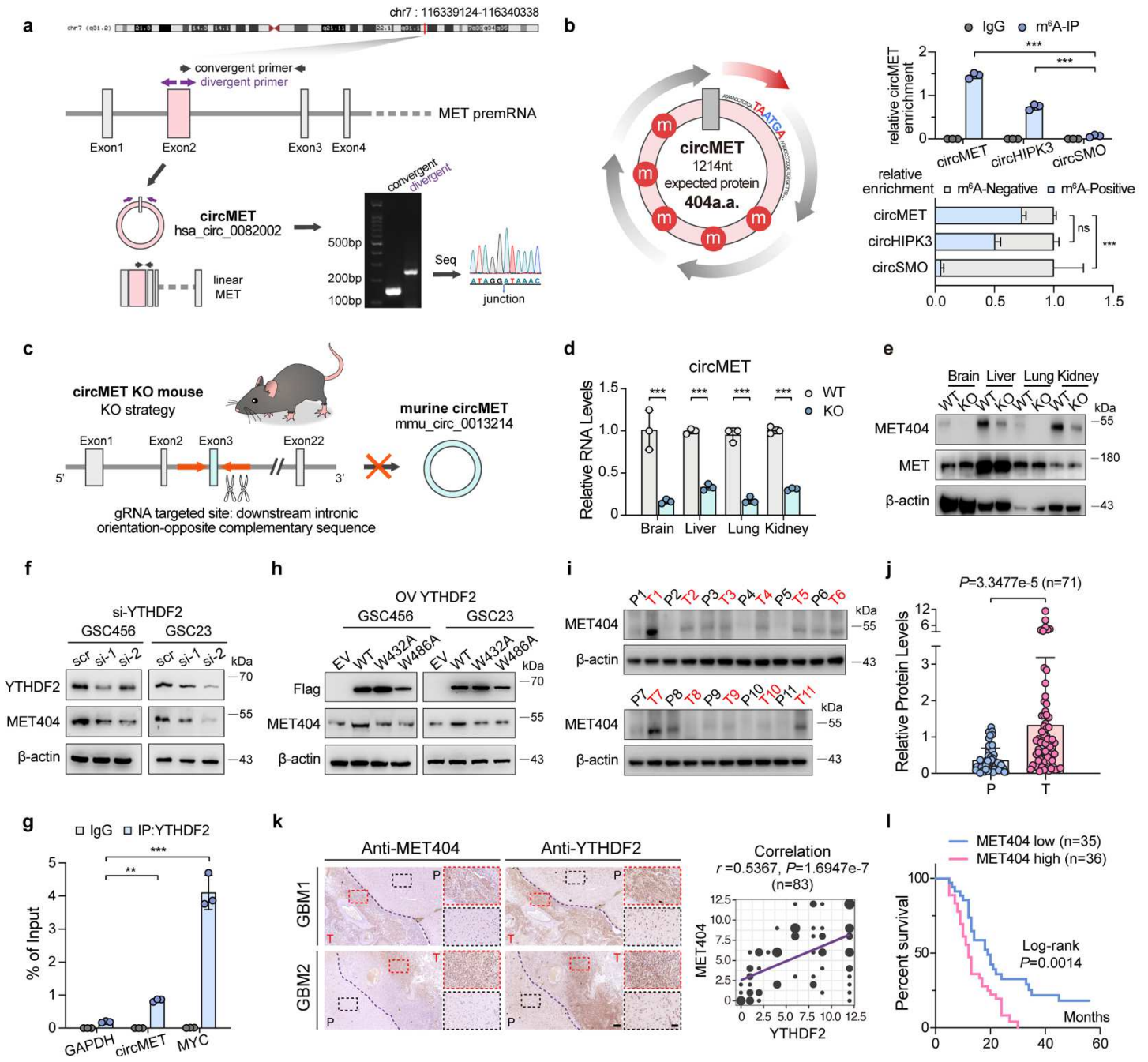


Figure 2. CircMET encodes a novel protein MET404 driven by the m⁶A reader YTHDF2

- 810 a. Illustration of the annotated genomic region of human circMET, different splicing forms of MET premRNA, and the validation strategy for the existence of circular MET exon 2. Convergent (black) and divergent (purple) primers were designed to amplify the linear or backspliced products. PCR analysis followed by Sanger sequencing using the indicated divergent primers revealed the “head-to-tail”
- 815 splicing of human MET exon 2.
- b. Left, illustration of the ORF and m⁶A modifications of circMET. Upper right, GSC23 cells were subjected to N⁶-methyladenosine immunoprecipitation (m⁶A IP) using an anti- m⁶A antibody or IgG control. Immunoprecipitates were analysed by RT–qPCR with specific primers for circMET, circHIPK3 (positive control) and
- 820 circSMO (negative control). Lower right, RNAs from the eluate (m⁶A positive) and supernatant (m⁶A negative) after m⁶A immunoprecipitation were purified and subjected to subsequent RT–qPCR analysis using the indicated primers.
- c. Schematic strategy of the circMET knock-out (KO) mouse model using CRISPR/Cas9 technology. Guide RNAs (gRNAs) were designed to target
- 825 downstream introns containing orientation-opposite complementary sequences that facilitate the circulation of exon 3 of mouse MET premRNA.
- d. CircMET RNA levels in the indicated organs of the circMET KO mouse model. Note that downstream intron deletion only reduced the circularization efficiency but could not completely abolish circMET expression.
- 830 e. Protein levels of MET404 and MET in the indicated organs of the wild-type (WT) and circMET KO mouse model.
- f. Protein levels of MET404 in YTHDF2-siRNA-transfected GSC456 and GSC23 cells.
- g. GSC23 cells were subjected to RNA immunoprecipitation using an anti-YTHDF2
- 835 antibody or IgG control and subsequent RT–qPCR analysis with specific primers for circMET, MYC (positive control) and GAPDH (negative control).
- h. Protein levels of MET404 in GSC456 and GSC23 cells transfected with empty

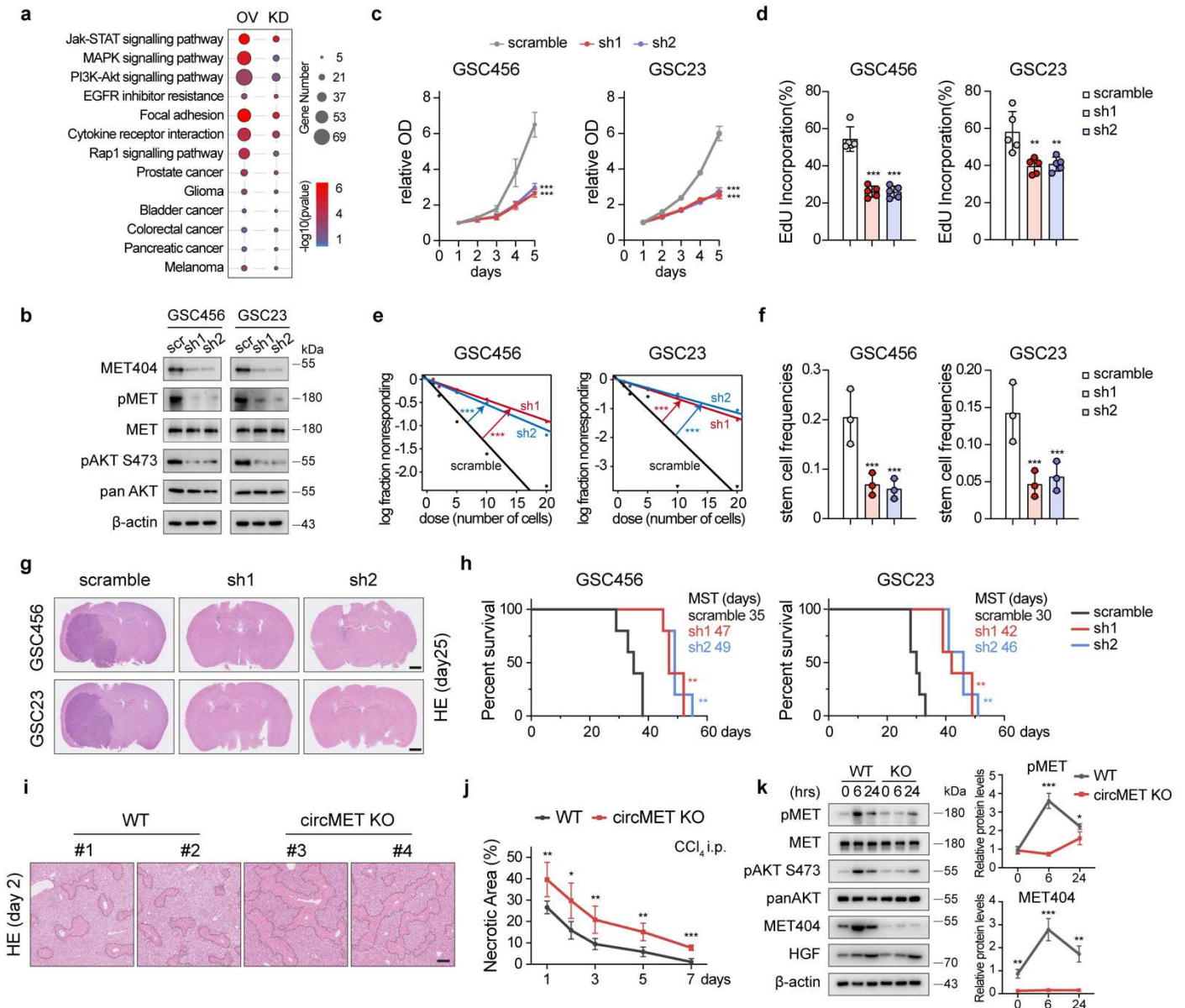
vector (EV), wild-type (WT) YTHDF2 or mutated YTHDF2 (W432A and W486A).

- 840 i. MET404 expression levels were measured in 11 randomly selected paired GBM samples using the custom anti-MET404 antibody.
- j. Semiquantitative analysis of MET404 expression levels based on immunoblot greyscale analysis in a GBM cohort of 71 samples. Paired t test, $P=3.3477e-5$.
- 845 k. Left, representative immunohistochemical (IHC) images showing the spatial correlation of MET404 and YTHDF2 from two GBM samples. The dark purple dashed lines indicate the border of the tumour. P, peritumour tissue. T, tumour. Scale bar, 250 μm . Inside the dashed box is the magnified view. Scale bar, 100 μm . Right, correlation analysis of MET404 and YTHDF2 expression levels based on IHC scores in a cohort of 83 GBM samples. $r=0.5367$, $P=1.6947e-7$.
- 850 l. Survival analysis of the aforementioned GBM cohort of 71 patients stratified by MET404 expression (with median expression level as the cut-off value). Log-rank test, $P=0.0014$.

The data in b, d-h are pooled from three independent experiments. The data are presented as the mean \pm SD. Unpaired two-tailed Student's t test was used to determine the significance of differences between the indicated groups where applicable. * $P<0.05$;

855 ** $P<0.01$; *** $P<0.001$.

Figure 3



860 **Figure 3. MET404 promoted GBM tumorigenesis by activating MET signalling**

a. Bubble plot of KEGG enrichment analysis based on bulk RNA-seq data of GSCs with stable knockdown (KD) or overexpression (OE).

b. Protein levels of phospho-MET and downstream phospho-AKT (S473) signals in circMET stable KD cells.

865 c. Proliferation of control and circMET stable KD GSC456 and GSC23 cells.

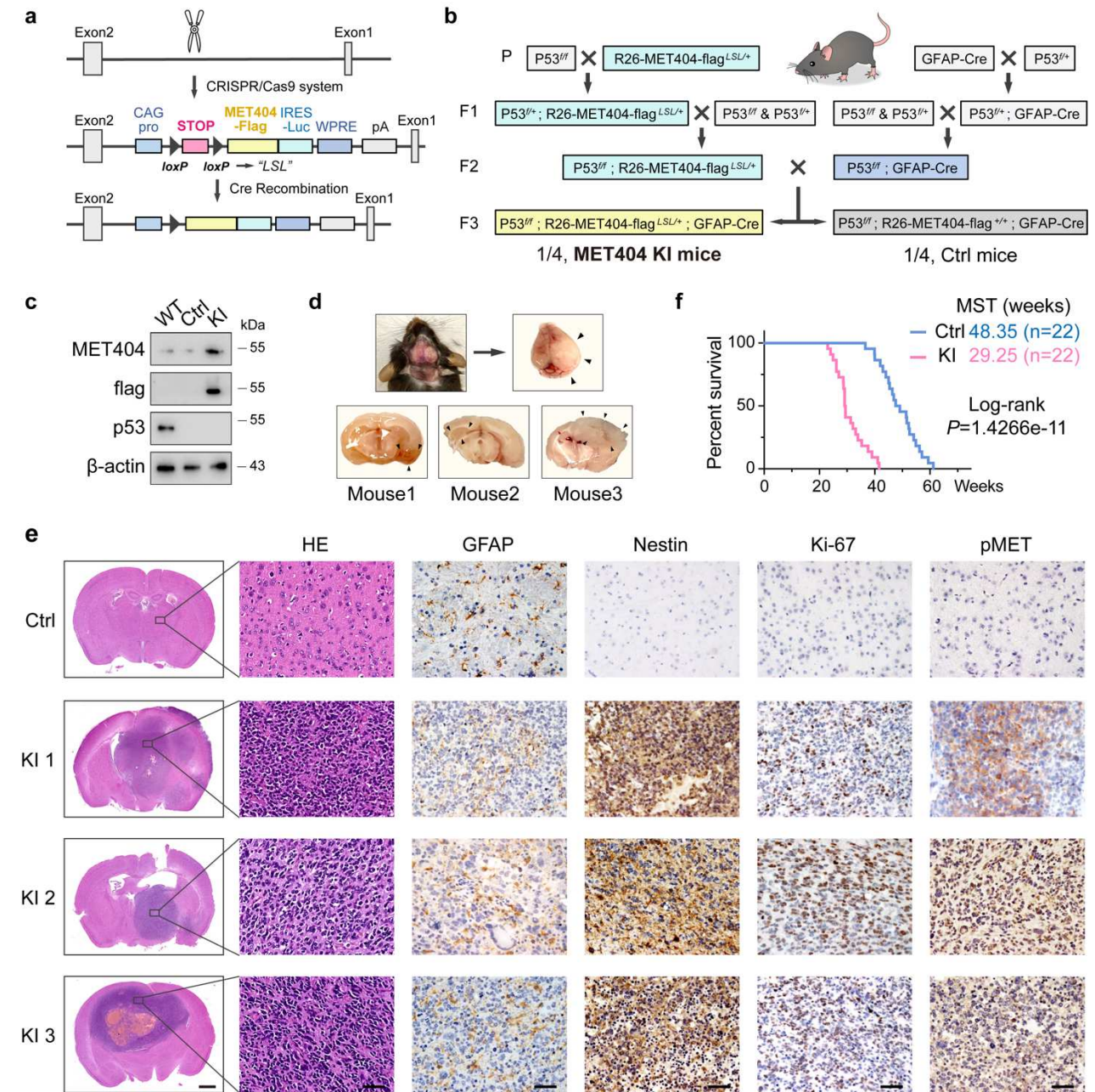
d. Quantification of the EdU incorporation assay of control and circMET stable KD GSC456 and GSC23 cells (n=5 randomly selected microscopic fields).

- e. Limited dilution assay (LDA) analysis of control and circMET stable KD GSC456 and GSC23 cells.
- 870 f. Stem cell frequencies of LDA analysis of control and circMET stable KD GSC456 and GSC23 cells.
- g. Representative haematoxylin and eosin (H&E)-stained brain slices from mice intracranially injected with control and circMET stable KD GSC456 and GSC23 cells. Scale bar, 1 mm.
- 875 h. Survival analysis of mice intracranially injected with control and circMET stable KD GSC456 and GSC23 cells (n=5 per group). Log-rank test, ** $P < 0.01$.
- i. Representative H&E-stained images of the CCl₄-induced acute liver injury model using wild-type or circMET KO mice on day 2. Dashed lines indicate the border of the necrotic area. Scale bar, 200 μ m.
- 880 j. Quantification of the liver necrotic area of the carbon tetrachloride (CCl₄)-induced acute liver injury model using wild-type or circMET KO mice (n=5 per group at each time point).
- k. Left, representative immunoblot of phospho-MET and downstream phospho-AKT (S473) in liver tissue collected at the indicated time points after intraperitoneal injection of CCl₄ in wild-type or circMET KO mice. Right, quantitative analysis of phospho-MET and MET404 protein levels in the left panel by greyscale analysis (n=3 per group at each time point).
- 885

The data are pooled from three independent experiments. The data are presented as the mean \pm SD. Unpaired two-tailed Student's t test was used to determine the significance of differences between the indicated groups where applicable. * $P < 0.05$; ** $P < 0.01$; *** $P < 0.001$.

890

Figure 4



8..

Figure 4. MET404 conditional knock-in initiated GBM in a genetic mouse model

- a. Schematic illustration of CRISPR/Cas9 system-mediated knock-in (KI) of MET404 at the mouse Rosa26 locus.
- 900 b. Illustration of the crossing strategy of the GBM spontaneous mouse model with conditional MET404 knock-in (MET404 KI mouse, $P53^{ff}$; $R26-MET404-flag^{LSL/+}$; $GFAP-Cre$) and control mice ($P53^{ff}$; $R26-MET404-flag^{+/+}$; $GFAP-Cre$). “+” means the wild-type allele, “f” denotes the conditional allele.
- c. Immunoblot of MET404-flag and p53 in brain tissues from the indicated mice.
905 Representative of three independent experiments.
- d. Upper left, representative photo of a MET404 KI mouse with a middle incision of its skull. Upper right, the swollen brain removed from the skull of the mouse on the left. Bottom, representative brain slice photo from three MET404 KI mice. Black arrows denote the edge of the tumour mass.
- 910 e. Representative H&E-stained and IHC images of MET404 KI and control mice using anti-GFAP, anti-Nestin, anti-Ki67 and anti-phospho-MET antibodies. Scale bar, 1 mm (for H&E-stained whole brain slices); 50 μ m (for enlarged H&E-stained brain slices and IHC images).
- f. Survival analysis of conditional MET404 KI and control mice (n=22 per group).
915 Log-rank test, $P=1.4266e-11$.

Figure 5

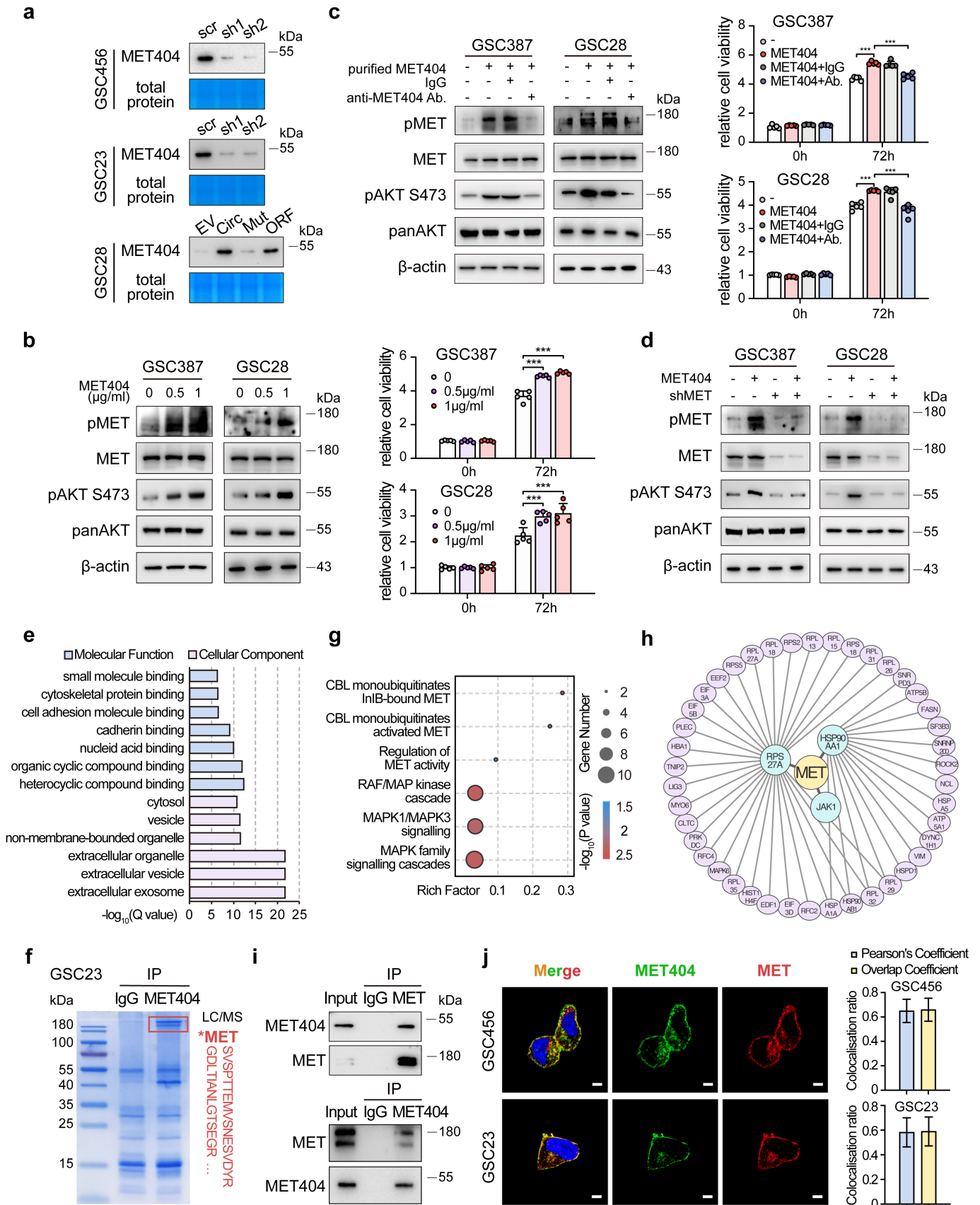


Figure 5. MET404 is a secreted protein that interacts with MET

- a. Immunoblot of concentrated supernatant from the culture medium of GSC456, GSC23 and GSC28 cells with the indicated modifications. EV, empty vector; Circ, stable OE of circMET; Mut, stable OE of circMET with insertion mutation; ORF, stable OE of linearized MET404 ORF vector. Coomassie blue-stained total proteins were used as a loading control.
- 925
- b. Left, protein levels of phospho-MET and downstream phospho-AKT (S473) in GSC387 and GSC28 cells after treatment with purified MET404 at the indicated concentrations. Right, proliferation of GSC387 and GSC28 cells with the indicated treatments.
- 930
- c. Left, protein levels of phospho-MET and downstream phospho-AKT (S473) in GSC387 and GSC28 cells treated with purified MET404 (1 $\mu\text{g/ml}$). Specific neutralizing MET404 antibody or IgG control was added as indicated. Right, proliferation of GSC387 and GSC28 cells with the indicated treatments.
- 935
- d. Protein levels of phospho-MET and downstream phospho-AKT (S473) in GSC387 and GSC28 cells with purified MET404 (1 $\mu\text{g/ml}$), MET stable KD or both.
- e. Gene Ontology analysis of candidate MET404 binding partners.
- f. Identification of MET sequences in GSC23 cells immunoprecipitated by an anti-MET antibody using mass spectrometry analysis.
- 940
- g. Reactome pathway analysis of candidate MET404 binding partners.
- h. Protein interaction network with MET as the hub generated by the STRING database based on candidate MET404 binding partners.
- i. GSC23 whole cell lysates were subjected to immunoprecipitation using anti-MET404 and anti-MET antibodies, followed by immunoblotting with anti-MET404 and anti-MET antibodies.
- 945
- j. Left, representative immunofluorescence images of the colocalization of MET404 and MET in GSC456 and GSC23 cells. Scale bar, 5 μm . Right, statistical analysis of GSC456 and GSC23 cells with MET404 and MET colocalization (n=30 randomly selected microscopy fields from three independent experiments).
- 950
- The data in a-d, i and j were pooled from three independent experiments. The data are presented as the mean \pm SD. Unpaired two-tailed Student's t test was used to determine the significance of differences between the indicated groups where applicable. * $P<0.05$; ** $P<0.01$; *** $P<0.001$.

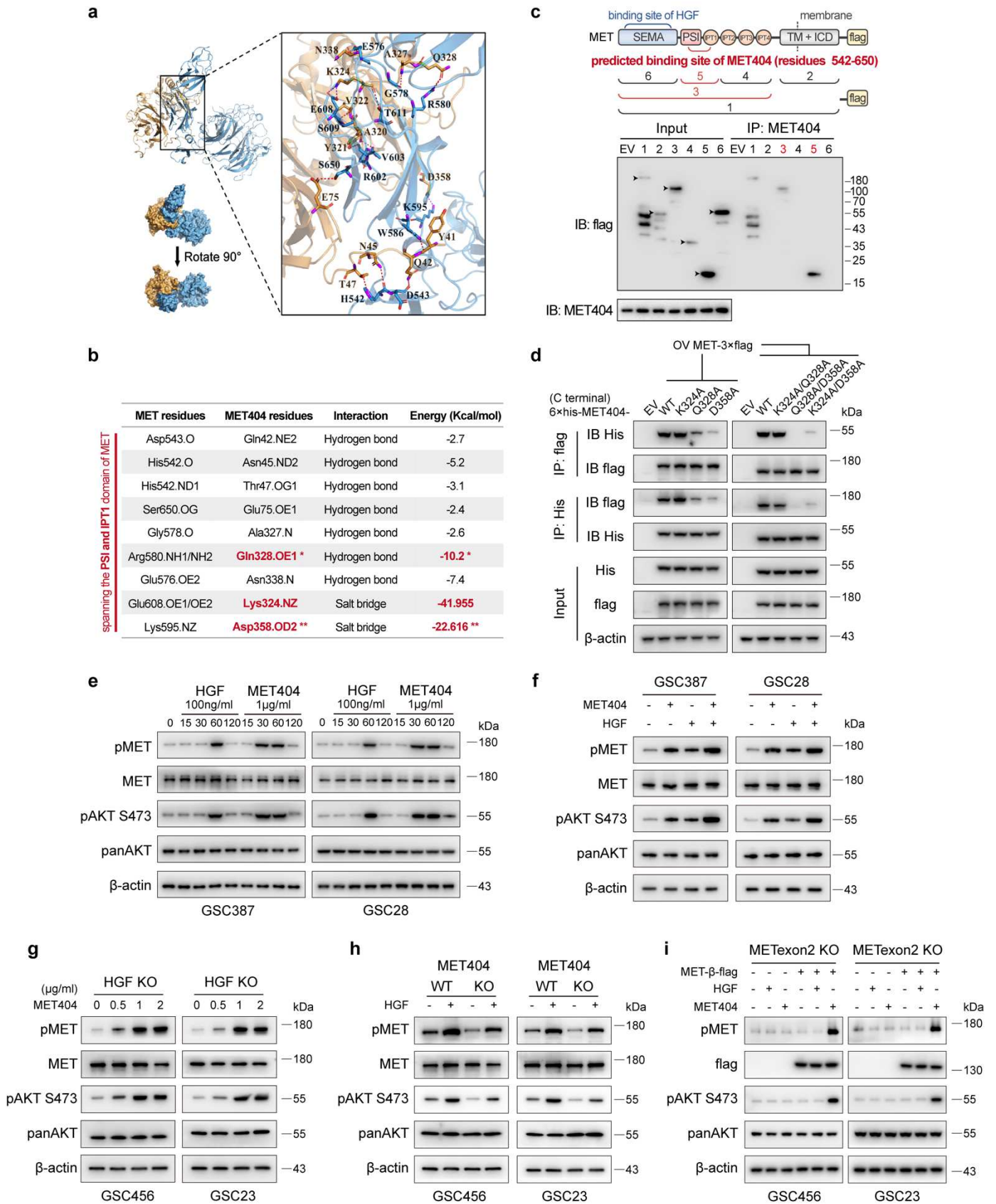


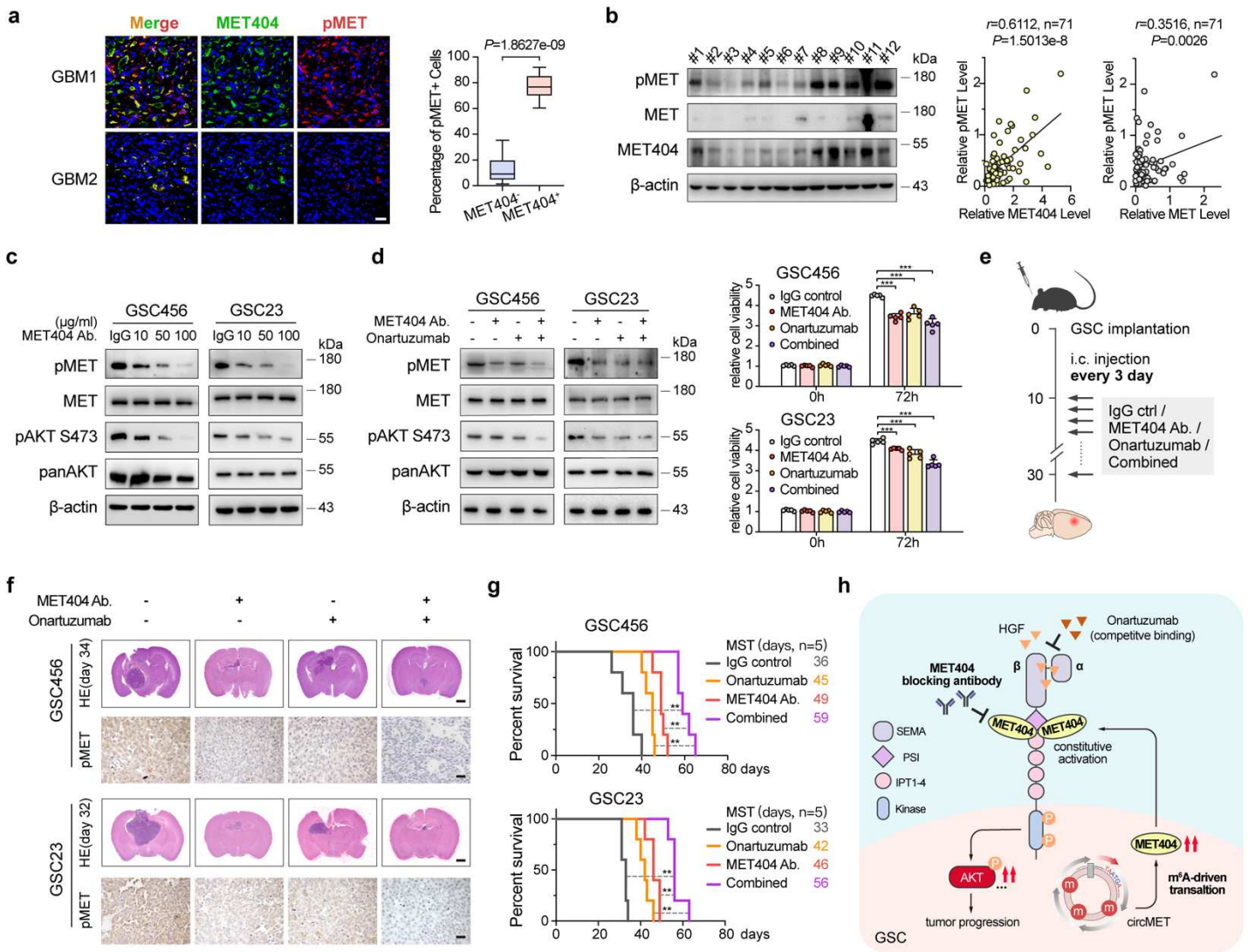
Figure 6. MET404 independently activates MET receptor

- a. Molecular docking analysis of MET404 and MET. Orange, MET404. Blue, MET.
- 960 b. The predicted amino acid contact list between MET404 and MET.
- c. Top, illustration of several truncations of full-length MET. Bottom, 293T cells were transfected with different Flag-tagged MET truncations. Cell lysates were immunoprecipitated with an anti-MET404 antibody, followed by immunoblotting with an anti-Flag antibody.
- 965 d. 293T cells were transfected with wild-type MET404, point-mutated MET404 (with a His tag at the C-terminus) or empty vector, along with flag-tagged MET. Whole-cell lysates were subjected to immunoprecipitation with anti-His or anti-flag antibodies, followed by immunoblotting with anti-His or anti-flag antibodies.
- e. Protein levels of phospho-MET and downstream phospho-AKT (S473) detected at
- 970 the indicated timepoints after stimulation with HGF or MET404 in GSC387 and GSC28 cells.
- f. Protein levels of phospho-MET and downstream phospho-AKT (S473) after one hour of stimulation with HGF (100 ng/ml), MET404 (1 μ g/ml) or both in GSC387 and GSC28 cells.
- 975 g. Protein levels of phospho-MET and downstream phospho-AKT (S473) with one-hour gradient stimulation of MET404 in GSC456 and GSC23 HGF KO cells.
- h. Protein levels of phospho-MET and downstream phospho-AKT (S473) in GSC456/GSC23 wild-type (WT) or MET404 KO cells with or without one hour of HGF stimulation (100 ng/ml).
- 980 i. HGF (100 ng/ml) or MET404 (1 μ g/ml) was used to treat METexon2 KO GSC456/GSC23 cells or those overexpressing the flag-tagged MET β subunit. Protein levels of phospho-MET and downstream phospho-AKT (S473) were detected in those cells.

The data in c-i are representative of three independent experiments.

985

Figure 7



990 **Figure 7. Synergistic effects of targeting MET404 and onartuzumab in restraining GBM progression**

a. Left, representative immunofluorescence images of MET404 and phospho-MET in GBM specimens. Scale bar, 30 μ m. Right, proportion of phospho-MET positive cells among MET404-positive or MET404-negative cells in 20 randomly selected microscopy fields of each immunofluorescence image ($n = 30$ independent GBM samples). Wilcoxon test, $P=1.8627e-09$.

995

b. Left, representative immunoblot of phospho-MET, MET and MET404 in 12 randomly selected GBM samples. Right, correlation analysis of MET404 vs.

- phospho-MET and MET vs. phospho-MET in a cohort of 71 GBM samples.
1000 $r=0.6112$, $P=1.5013e-8$ (MET404 vs. phospho-MET); $r=0.3516$, $P=0.0026$ (MET vs. phospho-MET).
- c. Protein levels of phospho-MET and downstream phospho-AKT (S473) in GSC456 and GSC23 cells after treatment with a specific MET404 antibody at the indicated concentrations. Representative of three independent experiments.
 - 1005 d. Left, protein levels of phospho-MET and downstream phospho-AKT (S473) in GSC456 and GSC23 cells treated with MET404 antibody, onartuzumab or both. Right panel, proliferation of GSC456 and GSC23 cells treated as indicated. Representative of three independent experiments. Unpaired two-tailed Student's t test was used to determine the significance of differences between the indicated
1010 groups. *** $P<0.001$.
 - e. Illustration of the *in situ* GBM model using nude mice treated with MET404, onartuzumab or combination therapy.
 - f. Representative H&E-stained brain slices and representative IHC images showing phospho-MET levels from mice implanted with GSC456 or GSC23 and treated with
1015 MET404, onartuzumab or both. Scale bar, 1 mm (H&E-stained brain slices) or 30 μm (IHC images).
 - g. Survival analysis of mice with the indicated therapeutic strategy (n=5 per group). Log-rank test, ** $P<0.01$.
 - h. Summary diagram of the whole study.

1020

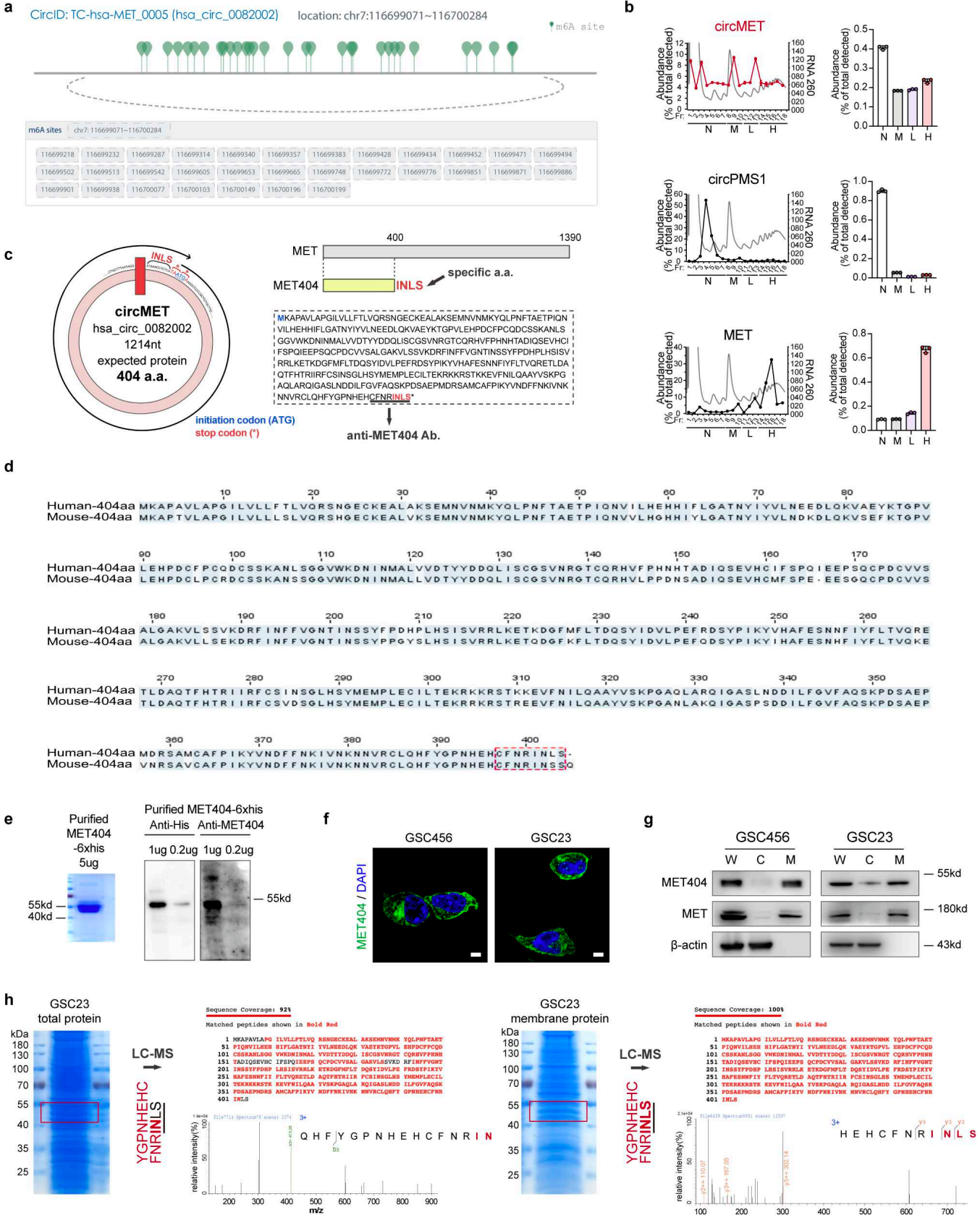
1025 **Extended Data Figure 1. M⁶A-seq of human glioma tissue; illustration of murine circMET; characteristics of human circMET.**

- a. Violin plot illustrating the expression level of m⁶A circRNAs and non m⁶A circRNAs in the 10 human glioma samples. Unpaired Student's t test, $P=0.019$.
- b. Illustration of the annotated genomic region of murine circMET. Exon 3 of murine
1030 MET pre-mRNA is backspliced into murine circMET (mmu_circ_0013214).
- c. Comparison of circMET sequences among humans, macaca, mice and rats. Green frame, start codon; red frame, stop codon.
- d. Relative RNA levels of circMET and MET in GSC23 cells with or without RNase R treatment.
- 1035 e. Oligo-dT or random primers were used to reverse-transcribe total RNA from GSC23 cells. Relative RNA levels of circMET and MET were measured by qPCR.
- f. Half-lives of circMET and MET mRNA after treatment with actinomycin D (2 $\mu\text{g/ml}$) in GSC23 cells.
- g. The RNA levels of circMET and MET were measured in cytoplasmic and nuclear
1040 fractions of GSC23 cells. β -actin and U6 were used as the cytoplasmic and nuclear controls, respectively.
- h. Relative RNA levels of circMET in NSC, NHA, GBM cell lines (U251, U118 and SNB19) and GSC cell lines.
- i. Left, illustration of shRNAs and FISH probes specific for the junction site of
1045 circMET. Right, representative images of FISH to detect circMET in GSCs. CircMET shRNAs were applied to verify the specificity of FISH probes. Scale bar, 10 μm .

The data in c-h were pooled from three independent experiments. The data are presented as the mean \pm SD.

1050

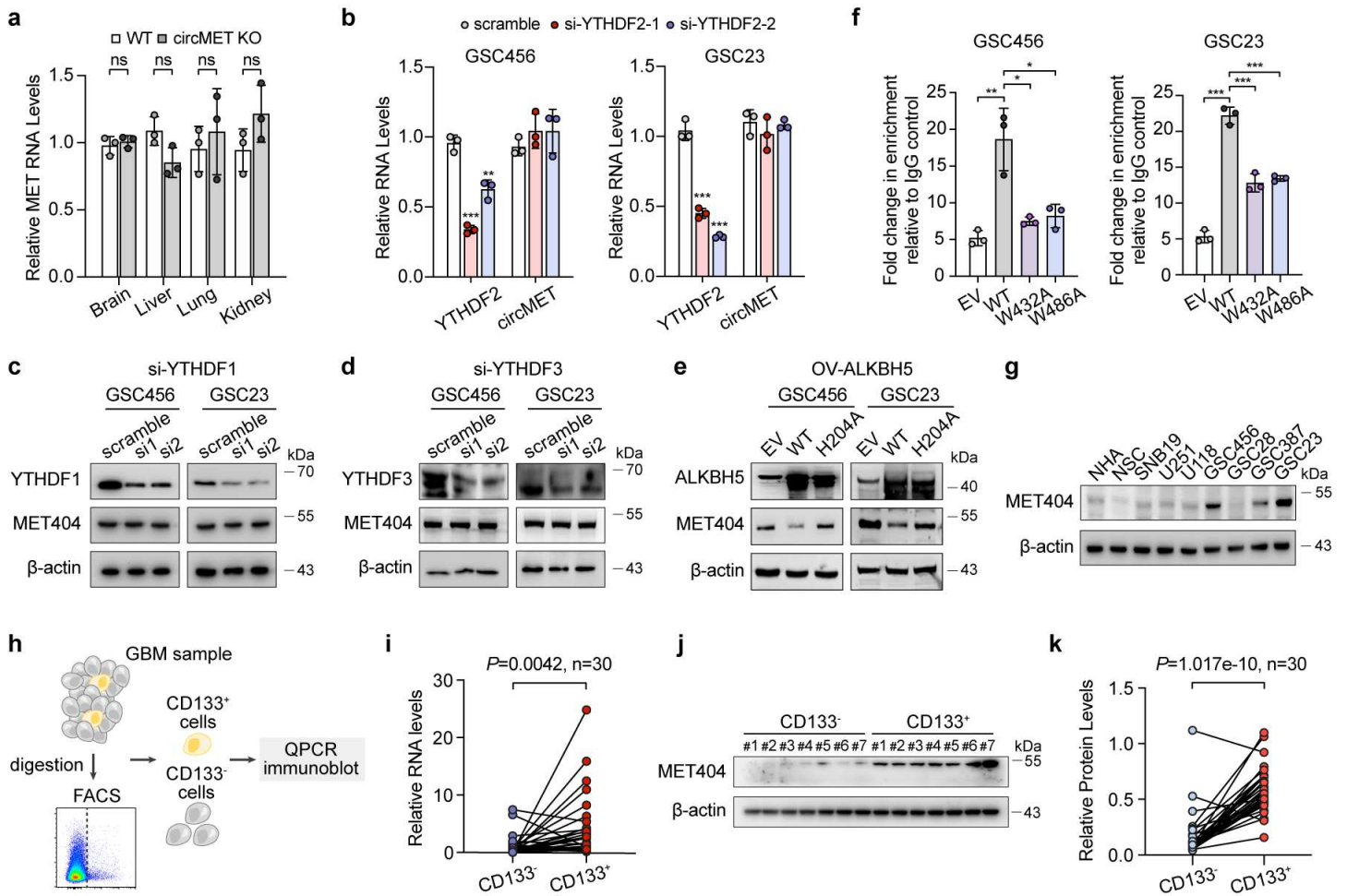
Extended Data Figure 2



- 1055 **Extended Data Figure 2. Characteristics of MET404 (related to Fig. 2)**
- a. Illustration of m⁶A-modified sites on circMET (hsa_circ_09226) adapted from the TransCirc database (<https://www.biosino.org/transcirc/search>).
 - b. Polysome profiling of circMET. CircMET levels were measured by qPCR of the indicated fractions. CircPMS1 and MET served as negative and positive controls,
1060 respectively. N, nonribosome; M, monosome; L, light polysome; H, heavy polysome. n=3 independent experiments.
 - c. Left, illustration of the circMET ORF with the unique C-terminus consisting of four amino acids (INLS). Right, comparison of amino acid sequences between MET404 and MET. Inside the dashed box is the full peptide sequence of MET404. A custom
1065 antibody was designed against the indicated unique C-terminus.
 - d. Comparison of the MET404 peptide sequence between humans and mice.
 - e. Left, Coomassie blue-stained purified MET404 with a C-terminal His tag. Right, immunoblot of purified MET404 using the custom anti-MET404 antibody. Representative of three independent experiments.
 - 1070 f. Representative immunofluorescence images of GSC456 and GSC23 stained with anti-MET404 antibody. Scale bar, 5 μ m.
 - g. Immunoblot for MET404, the membrane marker MET and the cytoplasmic marker β -actin in membrane/cytoplasmic fractionated GSC456 and GSC23 cells. Representative of three independent experiments. W, whole-cell lysate; C,
1075 cytoplasm; M, membrane.
 - h. Coomassie blue stained total protein (left) or membrane protein (right) of GSC23 cells. Proteins of the indicated molecular weight were collected for LC-MS analysis. Sequence coverage and detection of the unique C-terminal amino acids are shown to the right of the stained gel.

1080

Extended Data Figure 3



1085 **Extended Data Figure 3. CircMET-encoded MET404 is driven by the m⁶A reader YTHDF2 and is highly expressed in GSCs (related to Figure 2)**

- a. MET RNA levels in the indicated organs of the circMET KO mouse model.
 b. Relative RNA levels of YTHDF2 and circMET in GSC456/GSC23 cells transfected with YTHDF2 siRNAs.

1090 c. Protein levels of MET404 in GSC456/GSC23 cells transfected with YTHDF1 siRNAs.

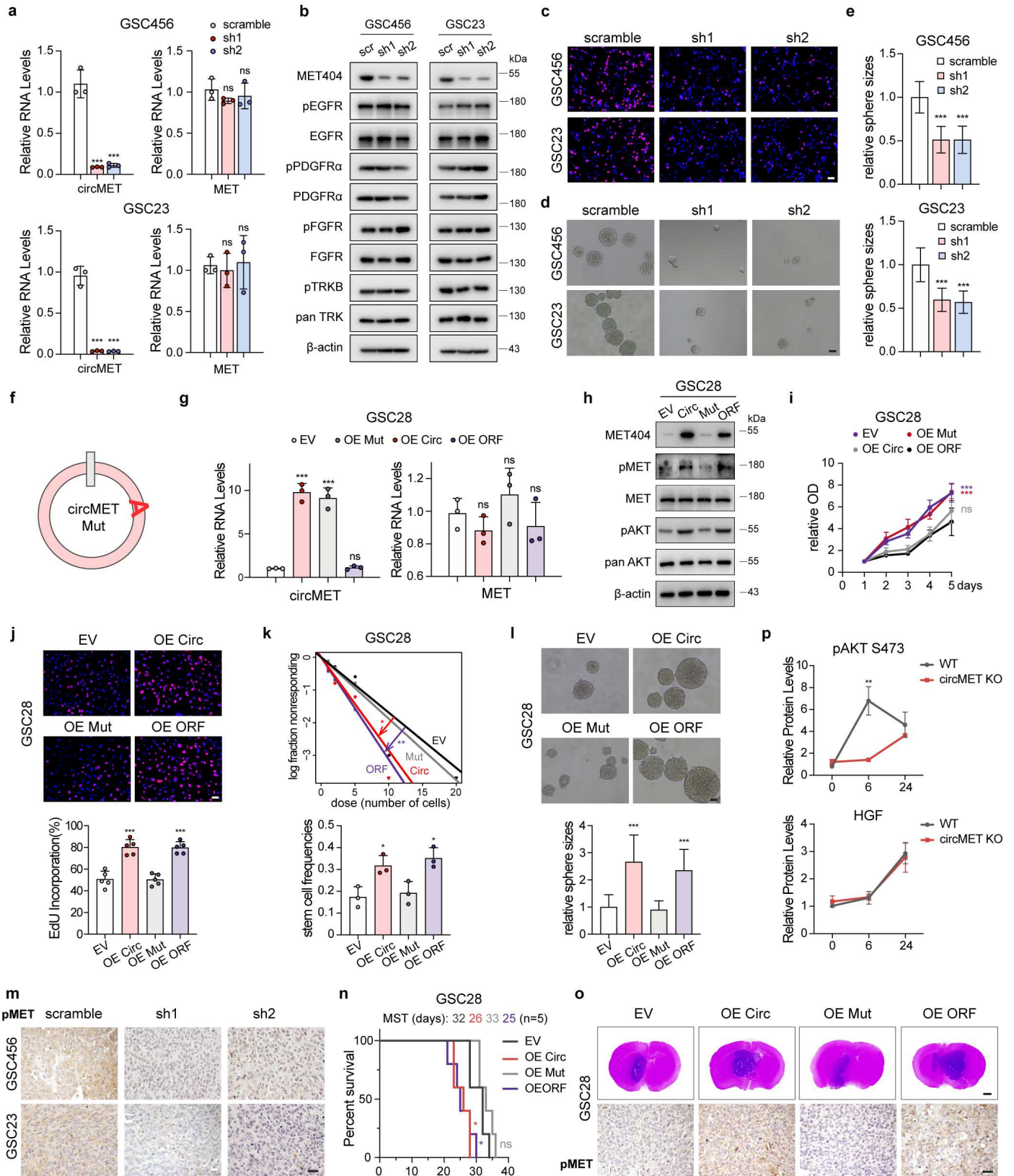
- d. Protein levels of MET404 in GSC456/GSC23 cells transfected with YTHDF3 siRNAs.

- e. Protein levels of MET404 in GSC456/GSC23 cells transfected with empty vector (EV), wild-type (WT) or mutated ALKBH5 (H204A).

1095

- f. GSCs transfected with empty vector (EV), wild-type YTHDF2 (WT) and mutated YTHDF2 (W432A and W486A) were subjected to RNA immunoprecipitation using anti-YTHDF2 antibody or IgG control and subsequent RT-qPCR analysis with circMET-specific primers.
- 1100 g. Protein levels of MET404 in NHA, NSC, GBM cell lines (U251, U118 and SNB19) and GSC cell lines.
- h. Illustration of CD133⁺ and CD133⁻ cell sorting from GBM tumour samples.
- i. Relative circMET RNA levels in CD133⁺ and CD133⁻ cells sorted from independent GBM samples (n=30). Paired t test, $P=0.0042$.
- 1105 j. Immunoblot of MET404 in CD133⁺ and CD133⁻ cells from 7 randomly chosen samples.
- k. Semiquantitative analysis of MET404 expression in CD133⁺ and CD133⁻ cells based on greyscale analysis in the same 30-patient GBM cohort. Paired t test, $P=1.017e-10$.
- 1110 The data in a-g were pooled from three independent experiments. The data are presented as the mean±SD. Unpaired two-tailed Student's t test was used to determine the significance of differences between the indicated groups where applicable. * $P<0.05$; ** $P<0.01$; *** $P<0.001$.

1115 Extended Data Figure 4



Extended Data Figure 4. MET404 boosted GBM tumorigenesis *in vitro* and *in vivo* (related to Fig. 3)

- 1120 a. Relative RNA levels of circMET and MET in GSC456/GSC23 cells with or without stable circMET KD.
- b. Protein levels of pEGFR, EGFR, pPDGFR α , PDGFR α , pFGFR, FGFR, pTRKB, and pan TRK in GSC456/GSC23 cells with or without stable circMET KD.
- c. Representative images of the EdU incorporation assay in control and circMET
- 1125 stably KD GSC456 and GSC23 cells. Scale bar, 50 μ m.
- d. Live cell images of GSC456/GSC23 cells with or without stable circMET KD. Scale bar, 50 μ m.
- e. Quantification of live cell images of GSC456/GSC23 cells with or without stable circMET KD.
- 1130 f. Illustration of mutated circMET construct with insertion of an adenine base.
- g. Relative RNA levels of circMET and MET in GSC28 cells with stable OE of empty vector (EV), circMET (Circ), mutated circMET (Mut), or MET404 ORF (ORF).
- h. Protein levels of phospho-MET and downstream phospho-AKT (S473) in GSC28 cells with the indicated modifications.
- 1135 i. Proliferation of GSC28 cells with the indicated modifications.
- j. Representative images (top) and quantification (bottom) of the EdU incorporation assay in GSC28 cells with the indicated modifications. Scale bar, 50 μ m.
- k. Top, limited dilution assay (LDA) analysis of GSC28 cells with the indicated modifications. Bottom, stem cell frequencies of LDA analysis of GSC28 cells with
- 1140 the indicated modifications.
- l. Live cell images (top) and corresponding (bottom) quantification of GSC28 cells with the indicated modifications. Scale bar, 50 μ m.
- m. Representative phospho-MET IHC images of brain slices in mice implanted with GSC456/GSC23 cells with or without stable circMET KD. Scale bar, 30 μ m.
- 1145 n. Survival analysis of mice implanted with GSC28 cells with the indicated modifications. Log-rank test, compared to EV group, * $P < 0.05$.

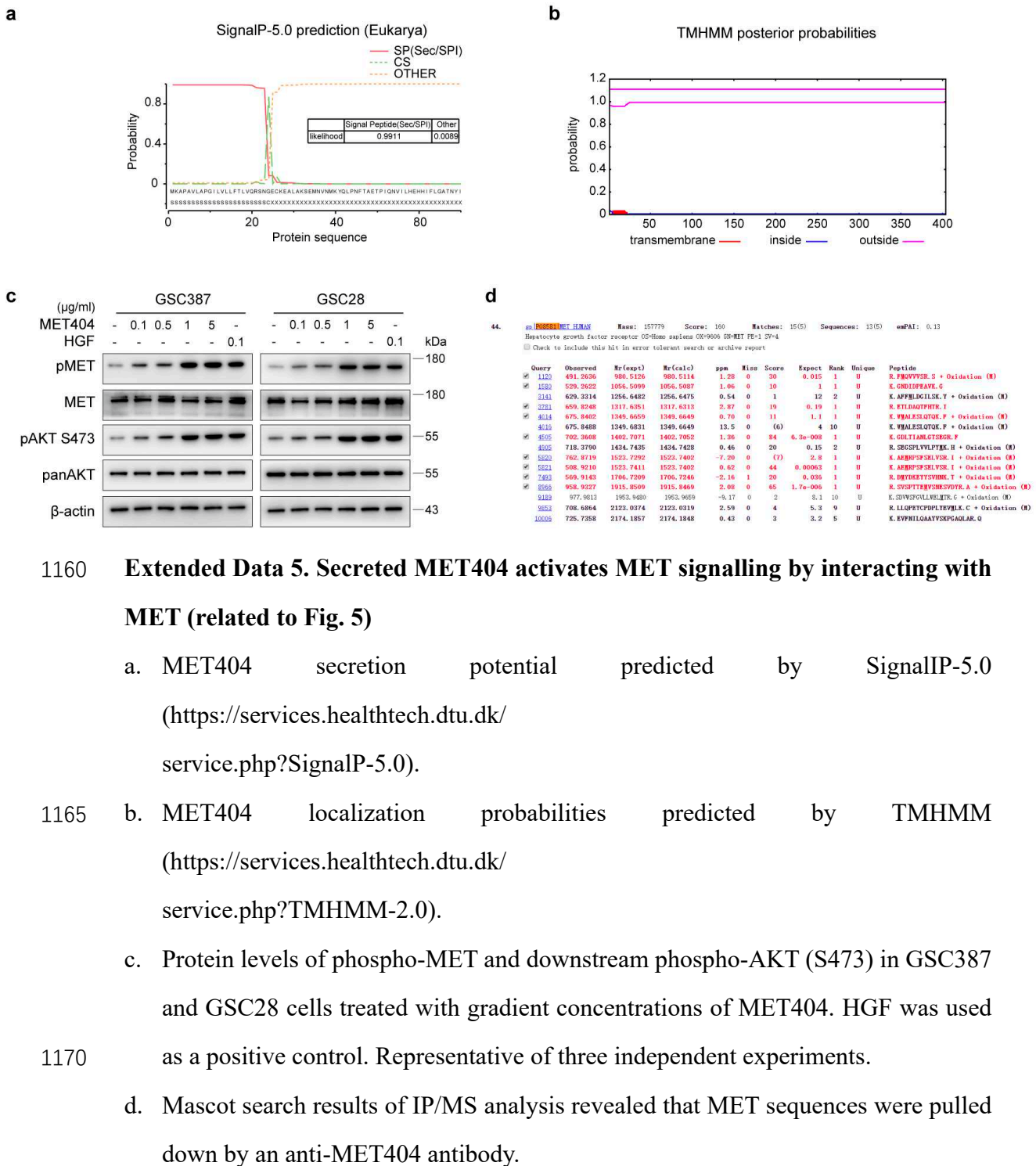
o. Top, representative H&E-stained brain slices of mice implanted with GSC28 cells with the indicated modifications. Scale bar, 1 mm. Bottom, representative phospho-MET IHC images from the same cohort of mice. Scale bar, 30 μ m.

1150 p. Quantitative analysis of phospho-AKT(S473) and HGF protein levels in the left panel of Fig.3k by greyscale analysis (n=3 per group at each time point).

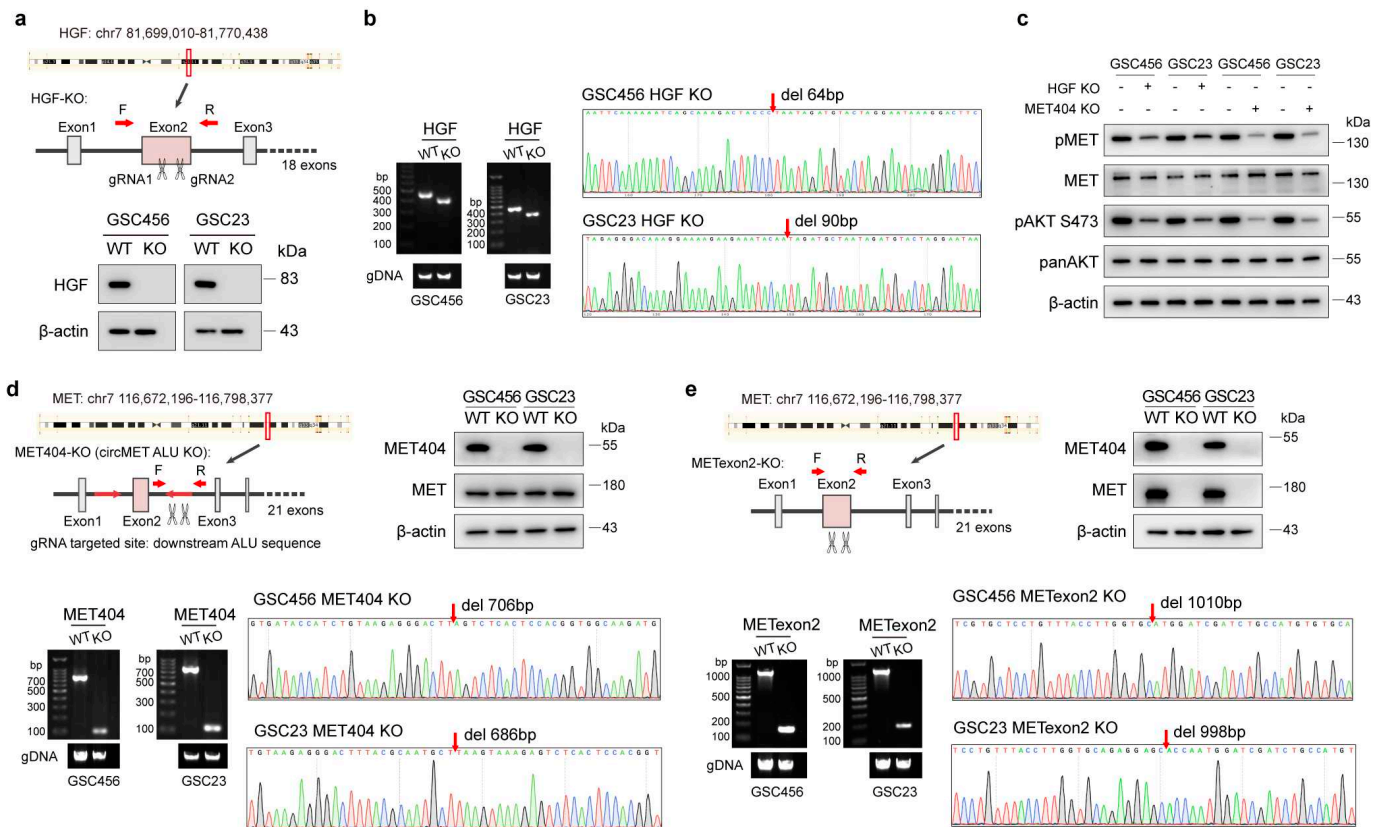
The data were pooled from three independent experiments. The data are presented as the mean \pm SD. Unpaired two-tailed Student's t test was used to determine the significance of differences between the indicated groups where applicable. * P <0.05;

1155 ** P <0.01; *** P <0.001.

Extended Data Figure 5



1175 **Extended Data Figure 6**



Extended Data Figure 6. Verification of KO cell lines and phospho-MET levels in KO cell lines (related to Fig. 6)

a. Top, CRISPR/Cas9-mediated HGF KO strategy and primer design for PCR validation. Bottom, immunoblot for HGF in wild-type (WT) or HGF KO GSC456/GSC23 cells.

b. Left, DNA gel electrophoresis of PCR for HGF in WT or HGF KO GSC456/GSC23 cells. Right, Sanger sequencing of PCR products for HGF in the indicated cells.

c. Protein levels of phospho-MET and downstream phospho-AKT (S473) in WT, HGF KO or MET404 KO GSC456/GSC23 cells.

d. Upper left, CRISPR/Cas9-mediated MET404 KO (circMET ALU KO) strategy and primer design for PCR validation. Upper right, immunoblot of MET404 in WT or MET404 KO GSC456/GSC23 cells. Lower left, DNA gel electrophoresis of PCR for the circMET downstream *Alu* sequence in WT or MET404 KO GSC456/GSC23 cells. Lower right, Sanger sequencing of PCR products for circMET downstream of the *Alu* sequence in the indicated cells.

1195 e. Upper left, CRISPR/Cas9-mediated MET exon 2 KO strategy and primer design for PCR validation. Upper right, immunoblot of MET404 and MET in WT or METexon2 KO GSC456/GSC23 cells. Lower left, DNA gel electrophoresis of PCR for MET exon 2 in WT or METexon 2 KO GSC456/GSC23 cells. Lower right, Sanger sequencing of PCR products for MET exon 2 in the indicated cells.

The data are representative of three independent experiments.

Supplementary Files

This is a list of supplementary files associated with this preprint. Click to download.

- [SuppTable1circRNAexpressionofm6Aseq.xlsx](#)
- [SuppTable2KEGGanalysisofm6AcircRNAsourcegenes.xlsx](#)
- [SuppTable3DEcircRNAsofRNCseq.xlsx](#)
- [SuppTable4circRNAexpressionofYTHDF2RIPseq.xlsx](#)
- [SuppTable5KEGGanalysisofRNAseqincircMETstablyOEorKDcells.xlsx](#)
- [SuppTable6CandidatebindingpartnersofMET404.xlsx](#)
- [SuppTable7ReactomepathwayanalysisofMET404bindingpartners.xlsx](#)
- [SuppTable8contactlistofdockinganalysis.xlsx](#)
- [SuppTable9primersoligosandprobes.xlsx](#)
- [20220614NCOMMS2222138nrreportingsummary.pdf](#)